Politecnico di Torino

Master's degree in Automotive Engineering

Integration and Kinematic Optimization of a Rotary Regenerative Shock Absorber for a Low Voltage Battery Electric Vehicle

Supervisors:

Prof. Nicola Amati
Prof. Andrea Tonoli
Dr. Giulia Moscone
Dr. Giorgio Bisciaio

Candidate:

Fabio Tassinari

Academic Year 2025/26

Abstract

The growing electrification of automotive systems is driving increasing interest toward suspension technologies that enhance ride comfort and road holding, while improving vehicle energy efficiency, enabling active control of vehicle dynamics, and the recovery of energy from road-induced excitations without requiring major changes to existing vehicle architectures. Within the objectives of the *"MOST Spoke 2: Sustainable Road Vehicles"* project, devoted to the development of lightweight, energy-efficient, and reconfigurable electric vehicles, the integration of an active suspension system represents a key step toward reducing the environmental, economic, and social impact of road transportation.

This thesis investigates the integration of a *Rotary Regenerative Shock Absorber* (RRSA), into the rear suspension of a low-voltage reconfigurable battery electric vehicle equipped with a conventional twist beam suspension layout. By replacing the original passive shock absorber, the proposed system converts the linear vertical motion of the suspension into rotational motion of an electric machine through a linkage mechanism and a compact gearbox, enabling the introduction of active and regenerative suspension functionalities through minimal modifications to the existing chassis and suspension architecture.

A systematic design methodology is developed to address the main challenges associated with this integration, including actuator placement, packaging constraints, kinematic compatibility, and force transmission efficiency. A three-dimensional analytical kinematic model is formulated to describe the suspension–actuator system over the entire suspension stroke. Functional and geometric requirements are translated into quantitative objectives and constraints, focusing on the optimization of the transmission ratio and transmission angle while preventing mechanical interferences with the surrounding components. A multi-objective genetic algorithm is then employed to explore the design space and identify optimal actuator placement and linkage configurations for two different mounting orientations of the rotary actuator. The optimization results are analyzed in terms of kinematic performance, mechanical feasibility, and energy conversion potential, leading to the selection of the final configuration that balances efficiency, compactness, and integration robustness.

Once the final configuration is selected, the linkage components are designed through CAD and FEM analyses to reduce the equivalent mass and moments of inertia, limiting potential NVH issues. The complete assembly kinematic and dynamic is finally evaluated in a multibody simulation environment and compared with the analytical model, confirming the validity and robustness of the proposed methodology.

Contents

List of Figures

List of Tables

Chapter 1

Introduction

Suspension systems play a fundamental role in vehicle dynamics, as they directly influence ride comfort, road holding, and handling stability. Traditionally, these objectives have been addressed through passive suspension architectures, which represent a well-established compromise between performance, robustness, and cost. However, passive systems are inherently limited in their ability to adapt to varying road conditions and driving scenarios, leading to a growing interest in controllable suspension technologies.

In recent years, the increasing electrification of automotive systems has further accelerated research on active and semi-active suspensions. On one hand, electrically actuated suspensions enable a more effective control of vehicle vertical dynamics, improving comfort and safety. On the other hand, they offer the opportunity to recover part of the mechanical energy that is conventionally dissipated by shock absorbers when the vehicle travels over uneven road surfaces. This energy, if properly harvested, can contribute to improving the overall efficiency of electrified vehicles, particularly in urban driving conditions where road-induced excitations are frequent. Despite their potential benefits, fully active suspension systems are still characterized by high complexity, significant power demand, and elevated costs, which limit their widespread adoption, especially in compact and low-cost electric vehicles. These limitations motivate the development of alternative solutions capable of introducing active and regenerative functionalities while preserving the simplicity of existing suspension and powertrain architectures.

Among the different technologies proposed in the literature, Rotary Regenerative Shock Absorbers (RRSA) offer several advantages in terms of energy conversion efficiency, bidirectional actuation capability, and controllability. By converting the linear motion of the suspension into the rotational motion of an electric machine through a gearbox and a linkage system, these devices can operate as both controllable dampers and as active force actuators. However, their integration into conventional vehicle suspensions remains a critical challenge, particularly for rear suspension layouts such as the twist beam, which are widely adopted in compact vehicles due to their simplicity, low cost, and packaging efficiency.

The main challenge lies in integrating a rotary actuator within a traditionally passive suspension architecture without requiring substantial modifications to the chassis or powertrain. Actuator placement, linkage geometry, packaging constraints, and kinematic compatibility must be carefully addressed to ensure efficient force transmission, adequate energy regeneration, and reliable operation throughout the full suspension stroke. Moreover, improper design choices may lead to increased unsprung mass, unfavorable inertia effects, or NVH issues, ultimately compromising vehicle performance. In this context, the objective of this thesis is to investigate the optimal integration of a rotary regenerative shock absorber into the rear twist beam suspension of a low-voltage reconfigurable battery electric vehicle within the objectives of the *"MOST Spoke 2: Sustainable Road Vehicles"* project. The project, developed in collaboration with the Mechanical Engineering Department of Politecnico di Torino, aims to design and develop lightweight, energy-efficient, and reconfigurable zero-emission road vehicles, minimizing their environmental, economic, and social impact over the entire lifecycle. A key aspect is the adoption of a low-voltage architecture, obtained by replacing the conventional high-voltage battery pack of a production Class A battery electric vehicle with a modular low-voltage energy storage system. This choice improves safety, reduces system complexity and cost, and facilitates integration with distributed energy and smart-grid infrastructures. However, the reduced available power and energy capacity makes efficiency-oriented solutions particularly critical. Within this framework, the integration of a regenerative and active suspension system represents a coherent and synergistic development. By harvesting part of the vibrational energy normally dissipated by passive dampers and enabling active control of vertical dynamics without major structural modifications, the proposed RRSA solution contributes to improving vehicle energy efficiency and functional versatility, while preserving the simplicity, compactness, and packaging advantages of the original twist beam layout. To achieve this goal, a systematic design methodology is developed, combining kinematic modeling, numerical solution techniques, and multi-objective optimization to identify feasible and efficient integration layouts.

The remainder of this thesis is organized as follows. Chapter 2 presents a review of suspension systems and controllable actuator technologies, with particular focus on regenerative and rotary electromagnetic shock absorbers. Chapter 3 describes the proposed design methodology, including the kinematic modeling of the suspension–actuator system and the optimization framework adopted for actuator integration. The subsequent chapters present the design, simulation, and validation of the final configuration, followed by conclusions and perspectives for future developments.

Chapter 2

State of art and background study

Suspension systems play a fundamental role in vehicle dynamics, as they directly influence ride comfort, road holding, and handling stability [1, 2, 3]. In recent years, significant research efforts have been devoted to improving these aspects through the development of advanced active suspension technologies equipped with mechatronic devices capable of generating controllable damping or even active forces within the suspension system [4], allowing also to perform regenerative shock absorption [5, 6].

This chapter provides an overview of the fundamental concepts and architectures of vehicle suspensions, with particular attention to the technological solutions relevant to the work presented in this thesis. The first part introduces the general principles and classifications of suspension systems [7, 8], while the final section focuses on active suspension actuators, including rotary regenerative shock absorbers [9].

2.1 Introduction to suspension systems

A vehicle suspension system is a mechanism that connects each wheel to the vehicle body or to a frame attached to it [1]. Since a rigid vehicle with more than three wheels would be a hyperstatic system, the vehicle structure must allow a certain degree of flexibility to maintain the contact between the wheels and the ground. This flexibility requirement is typically fulfilled by a set of deformable linkage systems, commonly known as suspensions, which serve two main purposes.
First, they must ensure the correct distribution of forces exchanged between the wheels and the ground under all load conditions, while also maintaining the proper vehicle trim. The introduction of a deformable linkage inevitably leads to geometric variations in the body position, which depend on the payload and its distribution. These variations are described through the coordinates of the center of gravity and the three body angles: yaw, roll, and pitch [2].
Second, suspensions must absorb and dissipate shocks transmitted from the road surface to the vehicle body. This requires a proper spring-damper system, since the elastic and damping properties of tires alone are insufficient to provide adequate comfort and handling, except at very low speeds on smooth surfaces [3].
Overall, suspensions are fundamental to achieve both handling and comfort, acting as a dynamic filter between the road and the vehicle body, limiting the amount of forces produced by road irregularities and maneuvers without compromising controllability.

2.1.1 Suspension systems architectures

From a structural point of view, suspensions are classified into three main categories [1]:

- **Independent suspensions**, where the two wheels on the same axle move independently, so a disturbance on one side does not affect the other.
  Examples include the *McPherson*, *Double wishbone*, *Trailing and Semi-Trailing arms*, and *Multilink* layouts.

- **Dependent suspensions**, where the two wheels are mechanically linked, meaning that the motion of one wheel influences the other. A typical example is the *Rigid guided axle* layout, although it is no longer used in modern vehicles.

- **Semi-independent suspensions**, which exhibit intermediate behavior between independent and dependent suspensions due to structural flexibility. The most commonly used type is the *Twist beam* layout, made up of two trailing or semi-trailing arms coupled with a torsion beam. This solution is widely adopted in the rear suspensions of compact cars.

A further distinction concerns steering and non-steering suspensions. Independent suspensions can be designed for steering axles, whereas dependent and semi-independent architectures are typically used on non-steering axles, except in specific cases such as heavy-duty or off-road vehicles.

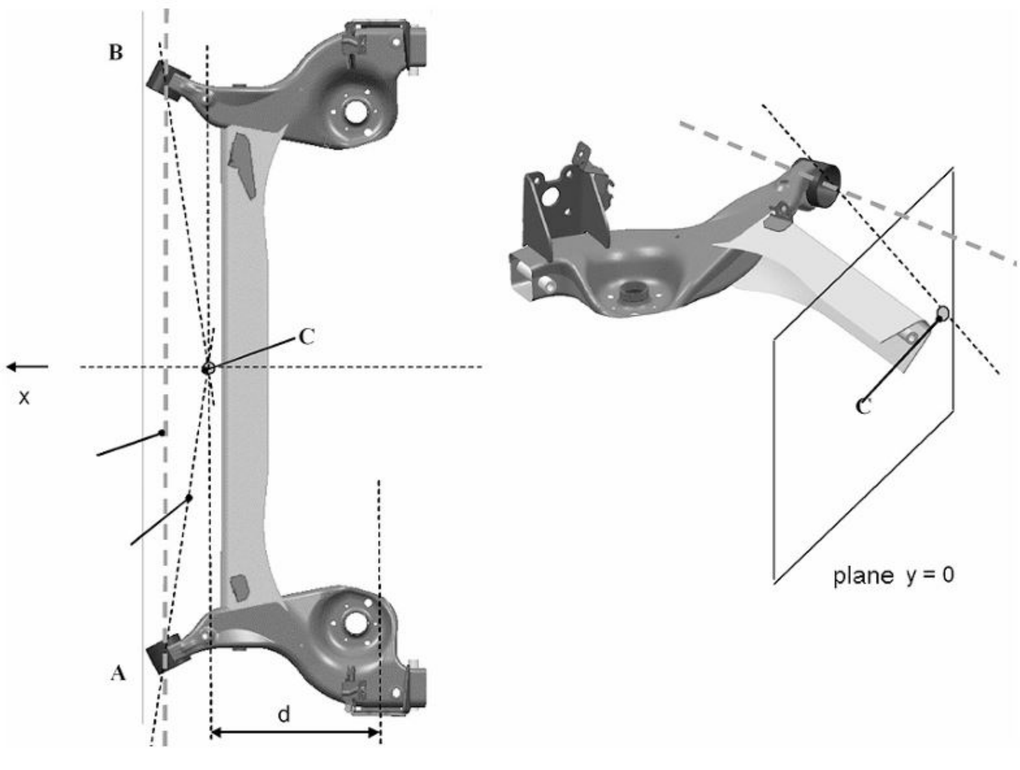

Figure 2.1: Twist beam suspension layout [1]

Regarding the semi-independent suspension twist beam layout, figure 2.1 shows the geometrical details of this configuration, since this will be the case of study for this thesis project. A and B represent the points where the suspension is hinged to the vehicle chassis, while point C represents the shear center of the cross section of the cross beam. The axis of rotation of the swing arms are tilted of a certain angle in the x-y plane to induce an understeering behavior in the car [1].

2.1.2 Suspension systems classification

Following the structural classification of suspensions presented in section 2.1.1, modern suspension systems can be subdivided in two main categories: passive suspensions and controllable suspensions (active or semi-active) [8].

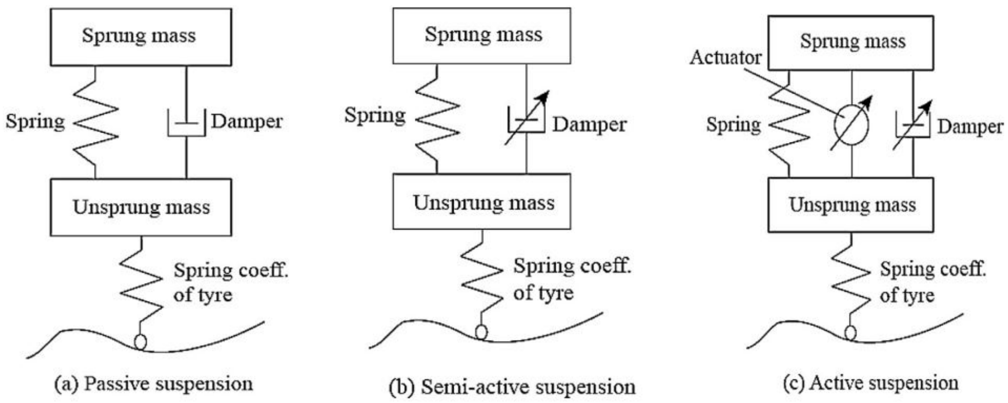

Figure 2.2: Quarter car schemes of passive, semi-active and active suspensions [7]

Passive suspensions represent the conventional approach, where the system is entirely mechanical: springs and dampers are fixed elements, and no active control of the suspension dynamic is possible. This configuration is simple, reliable, and stable, providing a fixed balance between ride comfort and road holding. However, their performance is limited, since they cannot actively control vehicle's body roll motion or wheel vertical dynamics to adapt to different road conditions.

Controllable suspensions introduce an external input that modifies the suspension behavior in response to vehicle dynamics. They can be described based on three main characteristics: the *controllability range*, which defines the range of forces that the actuators can deliver; the *control bandwidth*, indicating how quickly the actuator can respond; and the *power demand* (or *power request*), determined by the combination of force range and bandwidth.
Based on these characteristics, five families of controllable suspensions can be summarized as shown in Table 2.1:

- **Adaptive suspensions**: allows for a slow modulation of damping with a control bandwidth limited to a few Hertz. The power request is usually limited to a few Watts.

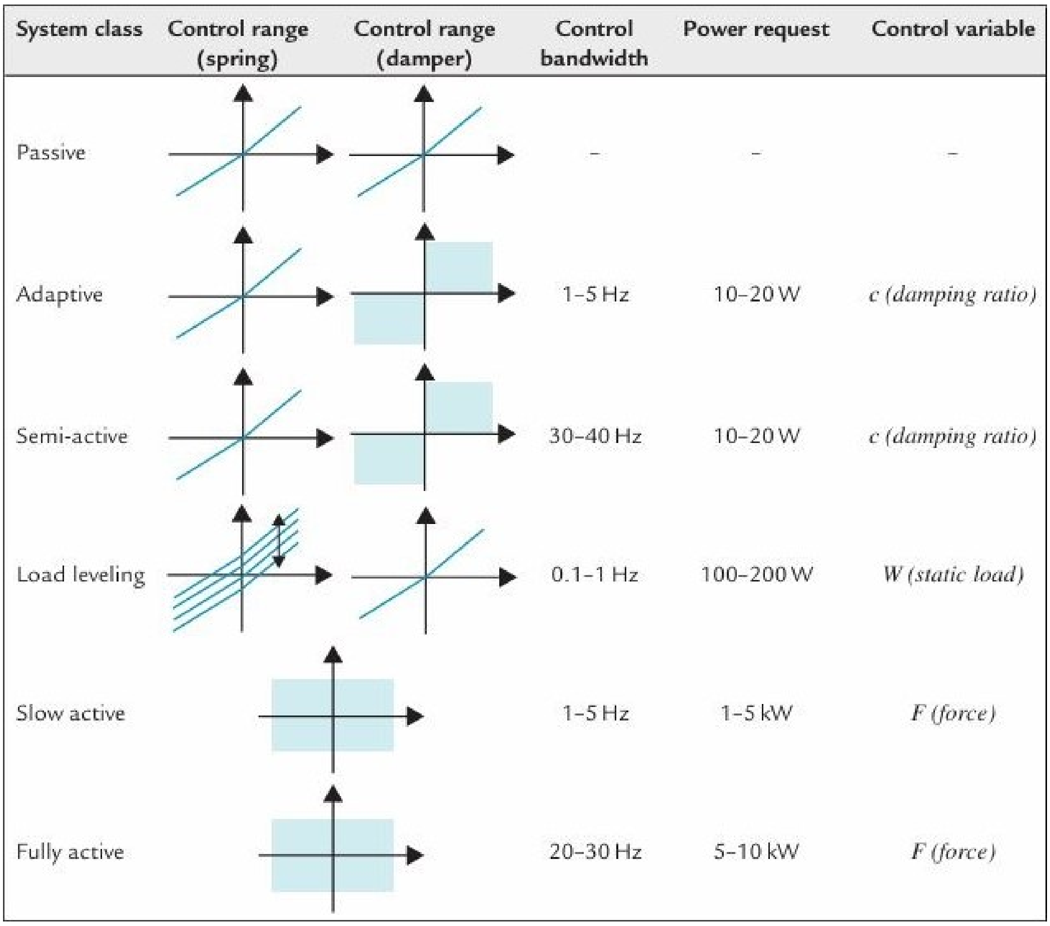

System class	Control range (spring)	Control range (damper)	Control bandwidth	Power request	Control variable
Passive			–	–	–
Adaptive			1–5 Hz	10–20 W	*c (damping ratio)*
Semi-active			30–40 Hz	10–20 W	*c (damping ratio)*
Load leveling			0.1–1 Hz	100–200 W	*W (static load)*
Slow active			1–5 Hz	1–5 kW	*F (force)*
Fully active			20–30 Hz	5–10 kW	*F (force)*

Table 2.1: Controllable suspensions classification [8]

- **Semi-active suspensions**: typically employ an electronic shock absorber capable of varying the damping over a relatively wide bandwidth, typically around 30–40 Hz. The power request is relatively low, around tens of Watts.

- **Load-leveling suspensions**: allows the introduction of energy into the system to regulate the static load. The control bandwidth is low, around 0.1–1 Hz, and the power demand is moderate, generally on the order of hundreds of Watts. These systems are effective for maintaining vehicle trim but have limited impact on the vertical dynamics of the body and wheels.

- **Slow-active suspensions**: replace passive elements with force actuators that can deliver a wide range of forces. The bandwidth is limited to a few Hertz, allowing for effective control of the body dynamics. However, the power requirements increase significantly, typically in the kilo-Watt range.

- **Fully-active suspensions**: combine a wide controllability range with high bandwidth, typically 20–30 Hz, enabling rapid reaction to road disturbances and vehicle dynamics. Similarly to the slow-active suspensions, fully-active ones introduce force actuators that can manage both body and wheel vertical dynamics, providing the highest potential performance. However, the associated power demand is substantial, on the order of tens of kilo-Watts.

Between all of these solutions, semi-active and fully-active suspensions can both influence the vehicle's vertical dynamics, but the latter have the potential to deliver the best performance due to their wider range of controllable forces. Although they have traditionally faced high energy demands and potential stability issues, modern control technologies enable more efficient operation and precise management of the system. These advances also enable effective energy-harvesting capabilities, further enhancing the appeal of fully-active suspensions for high-performance and energy-efficient applications.

2.2 Controllable suspension actuators

As described in section 2.1.2, controllable suspensions introduce an external input that modifies the suspension behavior in response to vehicle dynamics. This external input can be implemented through different types of actuators, usually named as shock absorbers, which may include variable damping systems or devices capable of delivering a variable amount of force.

Semi-active suspension actuators allowing fast variation of damping can be subdivided into three main technologies [8]:

- **Electrohydraulic (EH) dampers** (Figure 2.3a), in which the damping ratio is varied by acting on different electronic valves placed in the orifices of the piston.

- **Magnetorheological (MR) dampers** (Figure 2.3b), in which the damping ratio is varied by changing the viscosity of a mixture of oil and micro-particles sensitive to a controlled magnetic field generated by a coil at the orifices of the piston.

- **Electrorheological (ER) dampers** (Figure 2.3c), where the damping ratio is varied in a way similar to magnetorheological dampers but controlling the electric field instead of the magnetic one.

Fully-active suspension actuators, which are designed to supply active forces instead of just allowing damping variations, can be subdivided into two main categories [10]:

- **Hydraulic or pneumatic shock absorbers**, in which an hydraulic or pneumatic cylinder is powered by a pump (or a compressor) needed to pressurize the circuit, and a valve controls the amount of hydraulic or pneumatic energy necessary to create oscillatory-damping forces between sprung and unsprung masses. The main drawback of these systems is that they draw continuous power that is subsequently modulated and partially dissipated.

- **Electromagnetic shock absorbers**, which are made up of an electrical machine coupled to a transmission stage, either hydraulic or mechanical. This electrical machine can work as a generator when the device operates as a damper, and as a motor when it acts as an actuator. Consequently, compared to hydraulic or pneumatic shock absorbers, all the energy produced by the electric machine is directly used to generate forces instead of relying on a constant power source.

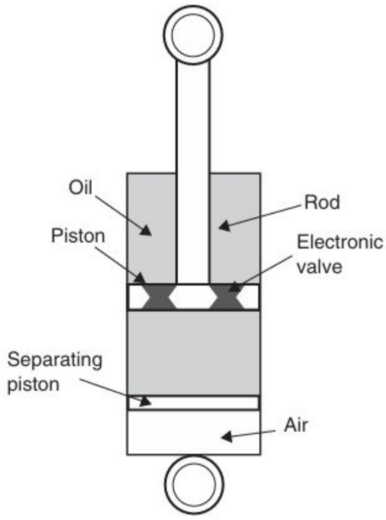

(a) Electrohydraulic (EH)

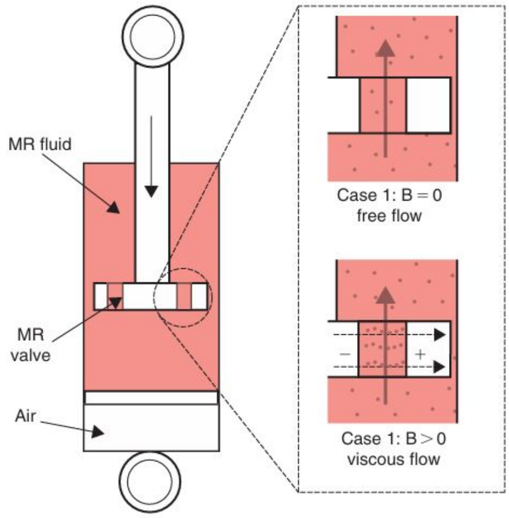

(b) Magnetorheological (MR)

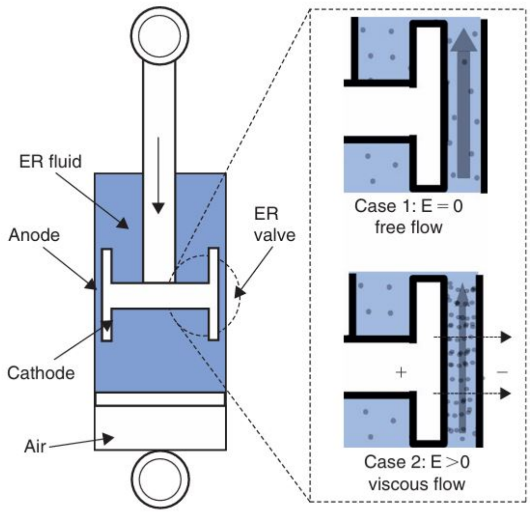

(c) Electrorheological (ER)

Figure 2.3: Semi-active shock absorber technologies [8]

Since electromagnetic shock absorbers can directly convert electrical energy into damping and actuation forces, instead of storing and partially dissipating it as in hydraulic or pneumatic systems, they offer higher efficiency and more precise force control. Depending on the transmission stage technology used, they can be classified into three types [10]: *linear*, *hydraulic*, and *rotary* (Figure 2.4).

Although linear electromagnetic shock absorbers (Figure 2.4a) are easy to integrate and feature a simple construction, their limited force density and poor damping capability make them unsuitable for demanding automotive applications. Hydraulic electromagnetic shock absorbers (Figure 2.3a) overcome these drawbacks through high force amplification, strong mechanical robustness, and low noise levels. However, they still experience substantial energy losses in valves, accumulators, and flow-rectification stages, which significantly reduce their overall conversion efficiency.

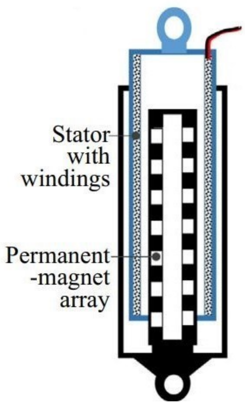

(a) Linear type

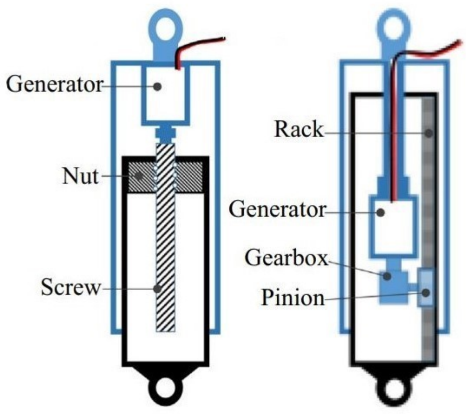

(b) Rotary type

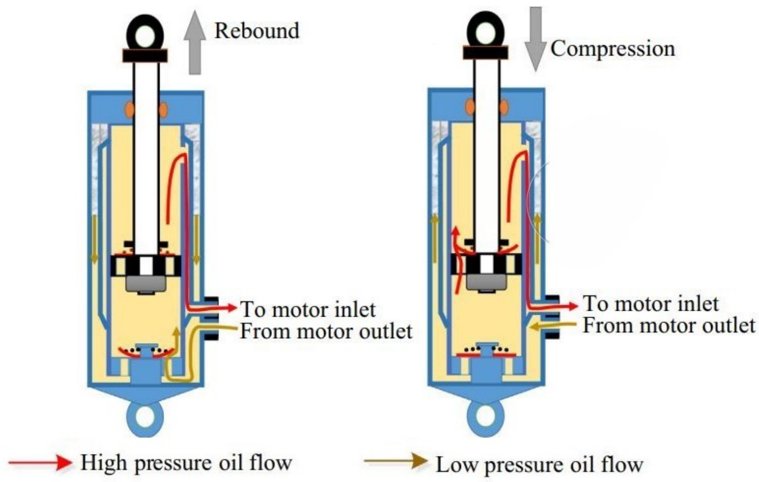

(c) Hydraulic type

Figure 2.4: Electromagnetic shock absorbers technologies [11]

Moreover, the rectifying mechanisms typically required prevent true bidirectional actuation, limiting their effectiveness for advanced active suspension controls. Rotary electromagnetic shock absorbers (Figure 2.4b) overcome many of the limitations of linear and hydraulic systems. By directly converting vertical suspension motion into bidirectional rotation, they eliminate working fluids and the associated losses, achieving high energy-conversion efficiency. Their efficiency, compact design, and control potential make them the most promising of the three technologies, as will be explored in more detail in section 2.2.1.

2.2.1 Rotary regenerative shock absorber - RRSA

Among the various electromagnetic shock absorber technologies shown in Figure 2.4, a specific research effort has been carried out at the *Department of Mechanical and Aerospace Engineering* of *Politecnico di Torino*, where a novel actuator prototype named *Rotary Regenerative Shock Absorber (RRSA)* has been developed [9]. This device converts the vertical linear motion of the suspension into rotary motion of a permanent magnet synchronous machine through a dedicated linkage mechanism and a compact high-ratio gearbox (Figure 2.5), introducing a total transmission ratio defined as $\tau_t = v_{wh}/w_m$. It can provide an active control force that aids or counteracts the suspension motion when the electric machine operates as a motor, or it can work as a controllable damper, converting the kinetic energy induced by road disturbances into electrical energy that can be stored in a battery. This latter functionality is also known as energy harvesting [12].

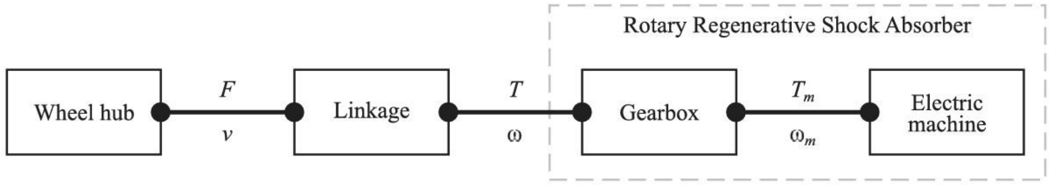

Figure 2.5: RRSA working principle diagram [9]

Compared to ball-screw and rack-pinion solutions, this system achieves higher efficiencies and control bandwidth, with a compact and lightweight layout, good mechanical robustness, and moderate additional inertia in the suspension resulting from the transmission ratio and the rotating inertia of the motor [13]. However, challenges derive from the noise level due to the presence of gearbox stages and from vehicle integration since additional space is needed to place the linkage while avoiding any contact with the vehicle chassis or other suspension components during the entire suspension stroke.

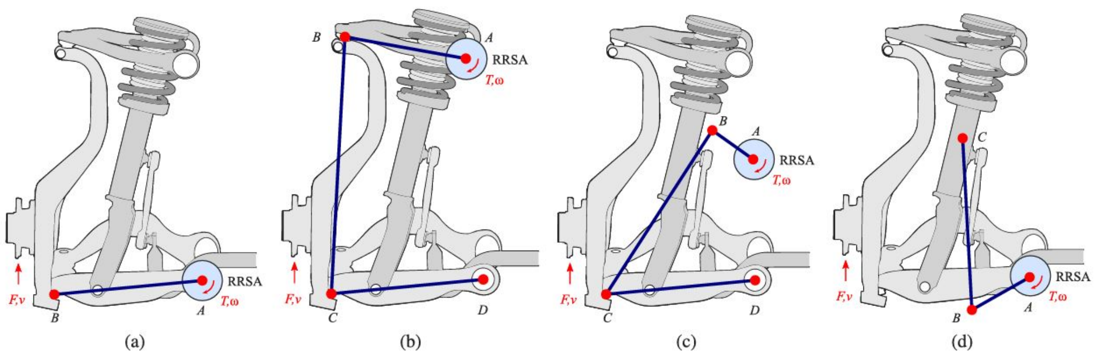

Figure 2.6: Proposed linkage solutions for RRSA integration into a double wishbone suspension layout [9]

According to the design methodology adopted for the RRSA, the linkage transmission ratio should be minimized to limit the contribution of the gearbox to the overall transmission ratio, thus reducing size, mass, and mechanical losses. Based on this criterion, several linkage configurations (Figure 2.6) were proposed and analyzed in the design of the first prototype, based on the system's integration into a double wishbone suspension layout [9]. Even if layout (c) leads to the lowest value of transmission ratio, layout (d) was selected as the most suitable compromise between a low transmission ratio and feasibility within the suspension layout, leading to a theoretical linkage transmission ratio $\tau_l = 115\ mm/rad$.

The selected value of τ_l allowed the definition of the electric machine by fixing the operating torque and speed ranges resulting from the suspension dynamics. Based on these requirements, a permanent magnet synchronous machine was designed to satisfy the damping specifications while ensuring compactness and thermal feasibility. Subsequently, a compact two-stage planetary gearbox was selected to achieve a high transmission ratio within a limited radial envelope, while ensuring adequate efficiency and load capacity. The gearbox transmission ratio was defined as $\tau_g = 1/87.35$, so that the combination of linkage and gearbox yields the required overall transmission ratio $\tau_t = \tau_l \tau_g$.
The final specifications of the first RRSA prototype are listed in Table 2.2, while the assembled prototype is shown in Figure 2.7.

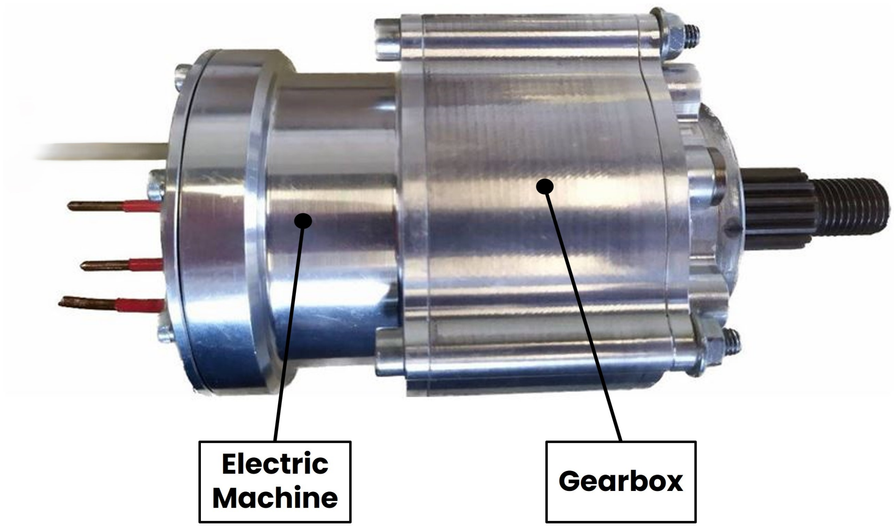

Figure 2.7: RRSA assembled prototype

Feature	**Symbol**	**Value**	**Unit**
DC link voltage	V_{DC}	48	V
Continuous motor torque	$T_{em,cont}$	0.7	Nm
Peak motor torque	$T_{em,max}$	2.7	Nm
Nominal linkage transmission ratio	τ_l	115	mm/rad
Gearbox transmission ratio	τ_g	1:87.35	-
Maximum suspension damping	$c_{s,max}$	10	kNs/m
Maximum suspension force	$F_{s,max}$	2	kN
Maximum suspension damping	$v_{s,max}$	2	m/s

Table 2.2: First RRSA prototype specifications [9]

Chapter 3

Design methodology

This thesis focuses on the integration of a rotary regenerative shock absorber [9] into the rear suspension of a low voltage reconfigurable battery electric city car equipped with a twist beam rear suspension layout [1]. The aim of this work is to adapt this actuator-based system to a traditionally passive suspension architecture, replacing the conventional shock absorber with the linkage-based solution described in Section 2.2.1. The integration of this system introduces additional design challenges, particularly related to actuator placement, suspension kinematics, packaging constraints, and energy conversion efficiency [9, 13]. In the context of a compact vehicle segment, preserving the simplicity and robustness of the twist beam suspension is a key requirement, making the actuator positioning a critical aspect of the overall system performance.

In this chapter, the proposed design methodology is presented. The process begins with the definition of design requirements for the integration of the rotary regenerative shock absorber, with particular emphasis on actuator positioning within the constraints of the suspension layout. Subsequently, a mathematical model is developed to describe the system behavior throughout the suspension stroke, capturing the kinematic relationships and energy conversion characteristics of the system. Finally, a constrained multi-objective optimization based on a genetic algorithm is performed to identify optimal actuator placement solutions that satisfy the design requirements, from which the final design configuration is selected.

3.1 Design requirements

This section defines the objectives, constraints, and performance targets for the integration of the rotary regenerative shock absorber into the rear twist beam suspension of the vehicle under study, providing the basis for subsequent mathematical modeling and optimization processes. In this context, design requirements can be broadly categorized into functional and geometric requirements, each addressing specific aspects of the system behavior, actuator positioning, and energy regeneration capability.

3.1.1 Functional requirements

The functional requirements define the expected behavior and performance of the rotary regenerative shock absorber integrated into the existing suspension layout. These requirements establish the functional objectives that the system must fulfill in order to enable active suspension behavior while ensuring effective energy regeneration from road-induced excitations [5, 6]. First, the integrated system shall be capable of introducing an active behavior into a traditionally passive suspension architecture. This includes the ability to modulate the damping characteristics of the rear suspension in response to operating conditions [4, 9], without compromising the simplicity and robustness of the twist beam suspension layout. In addition to active control capabilities, the system shall allow the recovery of mechanical energy generated by suspension motion. The effectiveness of this energy conversion is strongly influenced by the kinematic interaction between the suspension motion and the actuator [13]. Among the functional parameters governing this interaction, the *overall transmission ratio of the system* and the *transmission angle of the linkage* represent the most critical factors [14]. The overall transmission ratio τ_t can be defined as the ratio between the vertical velocity of the wheel hub and the rotational velocity of the electric machine. Under the assumption of negligible friction losses in the linkage joints, the power transmitted through the system can be considered constant ($P = T_{em}w_{em} = F_{v,wh}v_{wh} = const.$). As a result, the transmission ratio can be directly expressed in terms of torque of the electric machine and vertical force of at the wheel hub (eq. 3.1).

$$\tau_t = \frac{v_{wh}}{w_{em}} = \frac{T_{em}}{F_{v,wh}} \tag{3.1}$$

The transmission angle γ is defined as the angle between the lever arm and the push rod of the linkage [14], as shown in Figure 3.1. In the nominal position of the suspension (see Section 3.1.2), the transmission angle of the linkage should ideally be 90° to maximize the vertical force transmitted from the push rod to the actuator. This target value is considered during the optimization process to identify the most favorable actuator position and linkage configuration.

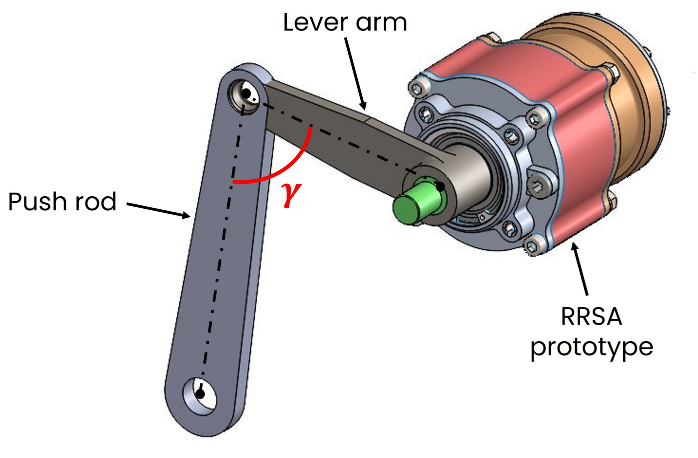

Figure 3.1: Transmission angle of the linkage

These parameters directly affect the force and velocity transmitted from the wheel hub to the RRSA, as well as the achievable torque, rotational speed, and power generation throughout the entire suspension stroke. The functional requirements thus define the target behavior of the system, guiding the development of the mathematical model and the subsequent optimization process.

3.1.2 Geometric requirements

The geometric requirements define the spatial and kinematic constraints governing the integration of the rotary regenerative shock absorber within the existing twist beam suspension layout, thus establishing the admissible design space by limiting component positions, orientations, and relative motions throughout the entire suspension travel. Figure 3.2 illustrates the geometry of the suspension in its reference or nominal position, corresponding to the static ride height of the vehicle.

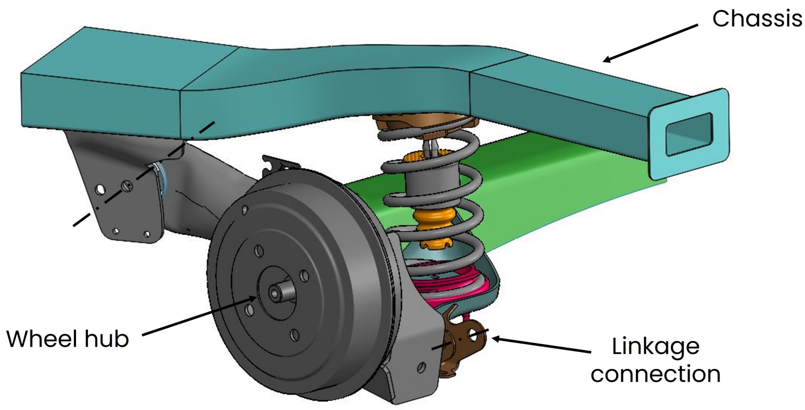

Figure 3.2: Twist beam suspension geometry (nominal position)

From this position, the suspension trailing arm ideally rotates around an axis of rotation tilted in the x-y plane, as stated in Section 2.1.1. The vertical displacement of the wheel hub resulting from this kinematic arrangement defines a total range from -52 mm to +48 mm with respect to the nominal configuration. This range represents the primary geometric constraint of the problem, as it directly defines the operating envelope within which the suspension components must operate, determining allowable lever arm lengths, joint positions, and overall packaging. Within this operating range, potential mechanical interferences between the linkage components and the wheel rim or vehicle chassis must be avoided. To satisfy this requirement, minimum clearance distances are imposed, consequently restricting the admissible positions and orientations of the linkage elements and further defining the feasible design space. In addition, in order to ensure adequate force transmission between the wheel hub and the actuator, the push rod must be placed as much vertical as possible. Finally, the placement of the rotary actuator must allow for secure attachment to the chassis via a flange, while maintaining sufficient proximity to avoid excessive stresses and reduce the risk of ground contact, thereby further constraining the admissible mounting positions.

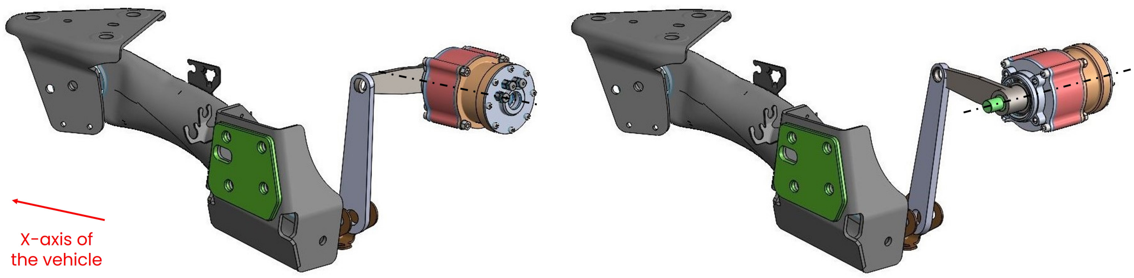

(a) (b)

Figure 3.3: RRSA possible mounting orientations

Within this constrained design space, two possible mounting orientations of the rotary regenerative shock absorber are considered. In the first configuration (Figure 3.3a), the actuator shaft is arranged parallel to the longitudinal axis of the vehicle, while in the second configuration (Figure 3.3b) the actuator shaft is oriented perpendicularly to it. The choice between these two different orientations for the final configuration of the system is discussed in the following sections.

3.2 Mathematical description of the system

In order to accurately describe the behavior of the suspension–actuator system, it is necessary to move from a qualitative understanding of the mechanism to a quantitative mathematical representation. The system can be considered as a set of rigid bodies interconnected by joints [15], whose relative positions and motions must be precisely defined throughout the suspension stroke. Closure equations are formulated based on the geometry of the linkage and the generalized coordinates of the mechanism [16], providing a complete description of the kinematics of the system and defining the relationships between wheel hub displacement, push rod position, and lever arm rotation, as well as transmission angle and transmission ratio. Due to the nonlinear nature of these equations, numerical solution methods [17] are required to determine the system configurations.

The following sections describe the formulation of the system equations, the specific assumptions applied to the twist-beam suspension and rotary actuator, and the numerical procedure used to solve the resulting non-linear system of equations.

3.2.1 Formulation of the closure equations

The mathematical formulation of the kinematic problem requires to express the closure conditions of the mechanism in analytical form. In their most general form, closure equations arise from the requirement that every vector loop constructed along the rigid bodies of the mechanism must geometrically close. For a generic loop of n rigid links, this condition can be written as:

$$\sum_{i=1}^{n} \vec{r_i} = 0 \tag{3.2}$$

where each vector $\vec{r_i}$ represents the position of a link as a function of its geometry and joint coordinates.

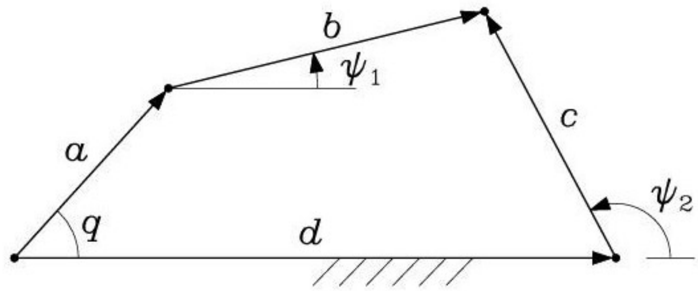

Figure 3.4: Planar four-bar linkage mechanism [16]

In classical planar mechanisms, such as the four-bar linkage (see Figure 3.4), closure relations involve only two spatial coordinates and are often solvable analytically, providing explicit expressions for the unknown joint angles. However, analytical solutions become too complex when the mechanism operates in three dimensions or involves multiple coupled variables. In the present case, the twist-beam suspension produces a spatial motion of the wheel hub due to its inclined rotation axis, while the rotary actuator can be mounted in a different orientation with respect to the vehicle reference frame. As a consequence, the closure relations must be formulated in a three-dimensional space, and multiple geometric constraints contribute to determining the admissible configuration of the mechanism. The resulting system of nonlinear trigonometric equations that cannot be solved algebraically must be solved through numerical methods [16, 17].

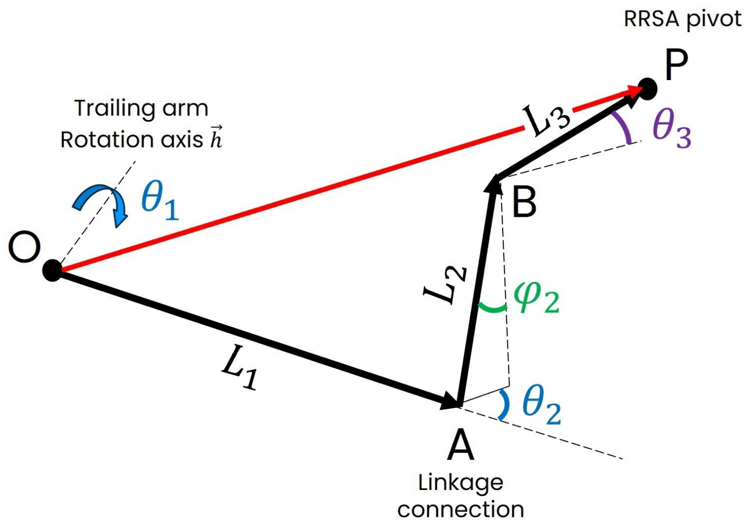

Figure 3.5: Mathematical description of the system

With reference to Figure 3.5, the configuration of this system can be fully described by a set of generalized coordinates that define the positions and orientations of the main links. The trailing arm L_1 rotates around an axis $\vec{h}$ inclined in the vehicle x-y plane through a revolute joint at point O, corresponding to its actual pivot and origin of the system; this rotation is represented by the coordinate θ_1. The push rod L_2 is connected to the trailing arm via a spherical joint at point A, whose position is uniquely determined by the rotation of the trailing arm. The position and orientation of the push rod L_2 is expressed in spherical coordinates, where θ_2 represents the rotation of the push rod in the x–y plane around the vertical z axis, and ϕ_2 defines its inclination relative to the z axis. The lever arm L_3 connects the end of the push rod at point B to the actuator at point P, closing the kinematic chain. Its orientation is defined by the coordinate θ_3, which represents the rotation of the lever arm around the revolute joint at P, with the axis of rotation aligned with the actuator shaft. The rotation of the trailing arm θ_1 is imposed by the vertical displacement of the wheel hub relative to its nominal position and represents the kinematic input of the system. For each value of θ_1, the positions of point A along the suspension stroke are calculated relative to the nominal coordinates $\vec{A}_{nom} = [A_x,\, A_y,\, A_z]^T_{nom}$ obtained from the CAD model of Figure 3.2, with respect to point O, by applying the Rodrigues rotation matrix around the trailing arm's rotation axis $\vec{h}$:

$$\vec{A}(\theta_1) = R(\theta_1, \vec{h})\, \vec{A}_{nom} \tag{3.3}$$

The remaining generalized coordinates θ_2, ϕ_2 and θ_3 are treated as unknowns to be solved from the closure equations of the system (see Equations 3.7, 3.8).

The general closure condition of a vector loop expressed in Equation 3.2, can be directly applied to the suspension–actuator mechanism. In this formulation, each link of the system is represented by a vector whose magnitude corresponds to the link length and whose direction is given by a unit vector along the link. Following the scheme depicted in Figure 3.5, the kinematic chain connecting points O, A, B and P can therefore be written as the sum of the oriented link vectors:

$$L_1\, \hat{u}_1 + L_2\, \hat{u}_2 + L_3\, \hat{u}_3 = \vec{OP} \tag{3.4}$$

where L_i is the magnitude of the i-th link, $\hat{u}_i$ is the corresponding unit vector defining its orientation, and $\vec{OP}$ is the vector that closes the loop from O to P. The first vector $L_1\, \hat{u}_1$, corresponds to the position of point A using the Rodrigues rotation matrix, as described in Equation 3.3. The unit vector of the push rod $\hat{u}_2$ can be expressed in Cartesian coordinates as a function of the unknown generalized coordinates θ_2 and ϕ_2:

$$\hat{u}_2 = \begin{bmatrix} \cos\theta_2 \sin\phi_2 \\ \sin\theta_2 \sin\phi_2 \\ \cos\phi_2 \end{bmatrix} \tag{3.5}$$

Similarly, the unit vector of the lever arm $\hat{u}_3$ is defined in Cartesian coordinates as a function of the unknown generalized coordinate θ_3, and depends on the possible orientation of the rotary actuator, with its axis oriented parallel or perpendicular to the longitudinal axis of the vehicle, as described in Section 3.1.2:

$$\hat{u}_{3,\parallel} = \begin{bmatrix} 0 \\ \cos\theta_3 \\ \sin\theta_3 \end{bmatrix}; \qquad \hat{u}_{3,\perp} = \begin{bmatrix} \cos\theta_3 \\ 0 \\ \sin\theta_3 \end{bmatrix} \tag{3.6}$$

By combining the Equations 3.4, 3.5 and 3.6, the closure condition of the mechanism can now be written explicitly in Cartesian form. Expanding the vector equation into its three components along the x, y and z axes yields a system of three nonlinear algebraic equations in the unknown generalized coordinates θ_2, ϕ_2 and θ_3. The form of the resulting closure equations depends on the orientation of the rotary actuator, due to the corresponding definition of the unit vector $\hat{u}_3$:

- **Parallel configuration**: the rotary actuator axis is aligned with the longitudinal axis of the vehicle. The closure equations are:

$$\begin{cases} A_x + L_2 \cos\theta_2 \sin\phi_2 = OP_x \\ A_y + L_2 \sin\theta_2 \sin\phi_2 + L_3 \cos\theta_3 = OP_y \\ A_z + L_2 \cos\phi_2 + L_3 \sin\theta_3 = OP_z \end{cases} \tag{3.7}$$

- **Perpendicular configuration**: the rotary actuator axis is perpendicular to the vehicle longitudinal axis. The closure equations are:

$$\begin{cases} A_x + L_2 \cos\theta_2 \sin\phi_2 + L_3 \cos\theta_3 = OP_x \\ A_y + L_2 \sin\theta_2 \sin\phi_2 = OP_y \\ A_z + L_2 \cos\phi_2 + L_3 \sin\theta_3 = OP_z \end{cases} \tag{3.8}$$

The next section presents the numerical procedure used to solve these systems of nonlinear equations and compute the complete kinematic configuration of the suspension–actuator system throughout the suspension stroke.

3.2.2 Newton Raphson method

Numerical methods are techniques by which mathematical problems are formulated so that they can be solved using arithmetic operations [17]. Despite the variety of such methods, they all involve extensive repetitive calculations, making them suitable only with the advent of fast and efficient digital computers. These methods are particularly useful for problems that are too complex to solve analytically, such as nonlinear algebraic equations arising in multibody kinematics.

In general, many engineering and scientific problems can be expressed as the task of finding the roots of a generic function $f(x)$, that is, the values of x for which $f(x) = 0$. Among the available techniques for root-finding, the *Newton–Raphson method* is widely used due to its simplicity, efficiency, and rapid convergence near a solution.

In one-dimension, given an initial guess x_0, the method iteratively updates the estimate solution x_{k+1} according to:

$$x_{k+1} = x_k - \frac{f(x_k)}{f'(x_k)}, \qquad k = 0, 1, 2, ... \tag{3.9}$$

Here, x_k represents the approximation of the root at the k-th iteration, and $f'(x_k)$ is the derivative of f evaluated in x_k. Geometrically, this procedure corresponds to drawing a tangent to the curve $y = f(x)$ at the current estimate x_k; the intersection of the tangent with the x-axis provides the next estimate solution x_{k+1}. The iteration is repeated until the difference between successive approximations is smaller than a fixed tolerance (see the example reported in Table 3.1).

k	x_k	$f(x_k)$
0	1.000000	1.000e+00
1	1.500000	2.500e-01
2	1.416667	6.944e-03
3	1.414215	6.007e-06
4	1.414213	4.511e-12

Table 3.1: Convergence of x_k using the Newton-Raphson method for $f(x) = x^2 - 2$

The main drawback of this method is that if the initial guess x_0 is too far from the true root, the tangent may intersect the x-axis in a region where the function behaves differently, potentially leading to divergence or convergence to an unintended root. Therefore, a reasonable initial guess is crucial to ensure the efficiency and reliability of the method. In the case of multiple dimensions and multiple unknowns, the Newton–Raphson idea can be extended to solve a system of n equations in n variables for which $F(x) = 0$, where:

$$F(x) = \begin{bmatrix} f_1(x_1, ..., x_n) \\ \vdots \\ f_n(x_1, ..., x_n) \end{bmatrix}; \qquad x = \begin{bmatrix} x_1 \\ \vdots \\ x_n \end{bmatrix} \tag{3.10}$$

Similarly to the one-dimensional case, the method seeks a correction that drives the residual vector $F(x)$ toward zero. The multidimensional Newton–Raphson iteration is obtained by linearizing F(x) around the current estimate x_k using a first-order Taylor expansion:

$$F(x_k + \Delta x) \approx F(x_k) + J(x_k)\,\Delta x \tag{3.11}$$

where $J(x_k)$ is the Jacobian matrix of the first derivaties:

$$J(x_k) = \begin{bmatrix} \dfrac{\partial F_1}{\partial x_1} & \cdots & \dfrac{\partial F_1}{\partial x_n} \\ \vdots & \ddots & \vdots \\ \dfrac{\partial F_n}{\partial x_1} & \cdots & \dfrac{\partial F_n}{\partial x_n} \end{bmatrix} \tag{3.12}$$

Unlike the one-dimensional case, where convergence can be monitored by the scalar value of $f(x_k)$, in the multidimensional scenario the convergence criterion is evaluated on the norm of the vector function $\|F(x_k)\|$, which provides a single measure of the residuals across all equations. This allows the algorithm to determine whether the system of equations is satisfied simultaneously in all dimensions, ensuring that the iterative process stops only when the solution meets the desired accuracy across the entire vector of unknowns. It is important to note that, in the multidimensional case, the value of Δx_k evaluated at each iteration can be retrieved by imposing $F(x_k + \Delta x_k) = 0$ in Equation 3.11, obtaining:

$$\Delta x_k = -J(x_k)^{-1} F(x_k) \tag{3.13}$$

Since this value relies on the invertibility of the Jacobian matrix at each iteration, if the Jacobian becomes singular or nearly singular, the iterative process may diverge or fail to converge to the correct solution. Furthermore, as in the one-dimensional case, the performance of the multidimensional Newton–Raphson method strongly depends on the choice of the initial guess x_0. Quadratic convergence is achieved only when the initial estimate is sufficiently close to the actual solution, whereas poor initialization may lead to divergence, stagnation, or convergence to an unintended root. This sensitivity to both the conditioning of the Jacobian matrix and the initial conditions represents one of the main limitations of this method in nonlinear multivariable settings and often motivates the adoption of auxiliary global strategies to improve robustness in practical applications. These considerations highlight the importance of a suitable initial guess and proper numerical safeguards when applying this method. The next section describes how the Newton–Raphson method is integrated into the solution procedure adopted in the present analysis.

3.2.3 Numerical solution of the closure equations

The nonlinear closure equations derived in Section 3.2 cannot be solved analytically and must therefore be treated using a numerical approach. To this end, the Newton–Raphson method is employed to determine the unknown generalized coordinates $x = [\theta_2, \phi_2, \theta_3]^T$ that satisfy the kinematic constraints for a fixed position of the trailing arm defined by $\vec{A}$. As a first step, the closure equations must be reformulated in a residual-based representation suitable for numerical solution. To this end, the known geometric terms are grouped together:

$$\vec{C} = \begin{cases} C_x = A_x - OP_x \\ C_y = A_y - OP_y \\ C_x = A_z - OP_z \end{cases} \tag{3.14}$$

In this way, the closure problem can be rewritten in the standard form $F(x) = 0$. Explicitly, the two configurations described by the Equations 3.7 and 3.8 can be written in matrix form as follows:

- **Parallel configuration**:

$$F_{\parallel}(\theta_2, \phi_2, \theta_3) = \begin{bmatrix} L_2 \cos\theta_2 \sin\phi_2 + C_x \\ L_2 \sin\theta_2 \sin\phi_2 + L_3 \cos\theta_3 + C_y \\ L_2 \cos\phi_2 + L_3 \sin\theta_3 + C_z \end{bmatrix} = 0 \tag{3.15}$$

- **Perpendicular configuration**:

$$F_{\perp}(\theta_2, \phi_2, \theta_3) = \begin{bmatrix} L_2 \cos\theta_2 \sin\phi_2 + L_3 \cos\theta_3 + C_x \\ L_2 \sin\theta_2 \sin\phi_2 + C_y \\ L_2 \cos\phi_2 + L_3 \sin\theta_3 + C_z \end{bmatrix} = 0 \tag{3.16}$$

As described in 3.2.2, a crucial aspect of applying the Newton–Raphson method is the choice of the initial guess x_0, which strongly affects convergence to the true roots of the problem. In this work, the initial guess is determined using a grid search over the admissible ranges of unknown variables [18].

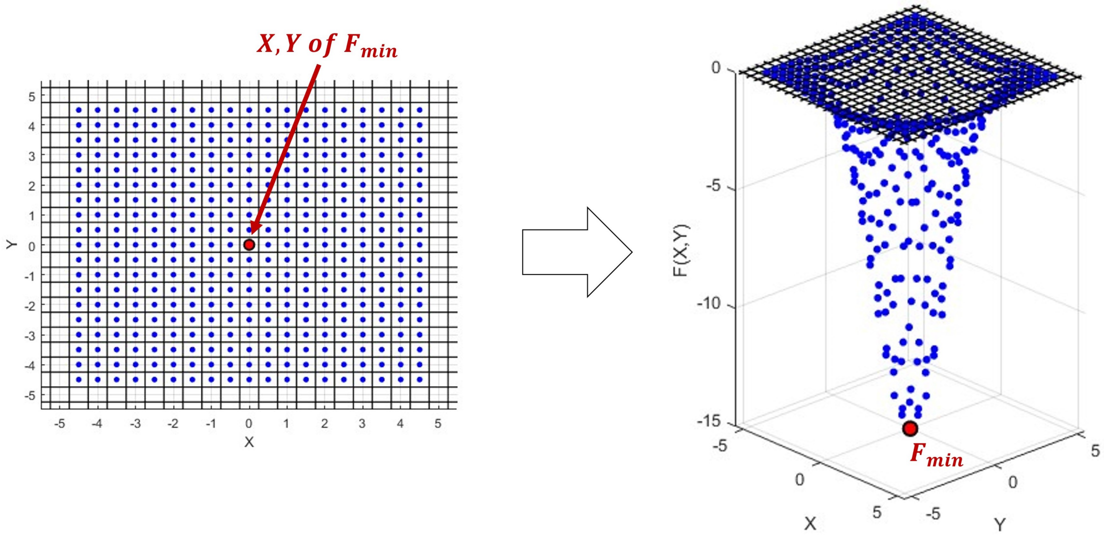

Figure 3.6: Grid Search on discretized X and Y for minimizing $F(X, Y)$

Grid search is a straightforward and systematic optimization method used to explore a multidimensional search space. The basic idea is to discretize the range of each variable into a finite set of values, forming a regular lattice of points in the parameter space. The objective function is then evaluated at each point of this lattice, and the point that yields to the best result according to a chosen criterion is selected, as shown in the example of Figure 3.6. Although this approach can be computationally intensive, it has the advantage of fully exploring the search space, reducing the risk of missing promising regions.

For the current kinematic analysis, a 3-D grid search is applied to determine an initial guess by discretizing the unknown generalized coordinates θ_2, ϕ_2 and θ_3 over their admissible ranges: $\theta_2 \in [0, 2\pi]$, $\phi_2 \in [0, \pi]$, $\theta_3 \in [0, 2\pi]$. In this implementation, a relatively coarse discretization of the variables is used to efficiently explore the search space. The function $F(\theta_2, \phi_2, \theta_3)$ is then evaluated at each point of the grid for each configuration of the system, and the combination of values that minimizes the chosen residual norm is selected as the starting point x_0 for the first Newton–Raphson iteration:

$$x_0 = [\theta_{2,0}, \phi_{2,0}, \theta_{3,0}]^T = \underset{\theta_2,\phi_2,\theta_3}{\arg\min} \|F(\theta_2, \phi_2, \theta_3)\| \tag{3.17}$$

This initialization strategy guarantees that the first iteration begins in a neighborhood of the true root, ensuring convergence of the method within a few steps. To show the effectiveness of this method, the kinematics of the system for both parallel and perpendicular rotary actuator configurations is solved in its nominal position, defined by $A_{nom} = [462.06,\ 5.86,\ -93.93]^T$. Table 3.2 reports the lengths of links L_2 and L_3 and the coordinates of point P, used as reference values for this calculation.

Link/Joint	**Value $\parallel$ [mm]**	**Value $\perp$ [mm]**
L_2	150	170
L_3	110	130
P_x	460	575
P_y	100	5
P_z	60	70

Table 3.2: Reference values of L_2, L_3 and P for nominal kinematic solutions in parallel and perpendicular configurations

Starting from the initial guess obtained through the coarse grid search, the iterative Newton–Raphson procedure updates the unknown coordinates until convergence is achieved within a fixed tolerance on the residual norm of 10^{-12}. The results of both configurations are reported in Tables 3.3 and 3.4.

Parallel Configuration (nominal position)				
k	$\theta_{2,k}$	$\phi_{2,k}$	$\theta_{3,k}$	$\|F(x_k)\|$
0	263.9430°	6.1053°	2.4655°	5.999e+00
1	262.5572°	6.0817°	2.4892°	3.937e-01
2	262.5521°	6.0835°	2.4895°	4.884e-03
3	262.5521°	6.0835°	2.4895°	4.256e-07
4	262.5521°	6.0835°	2.4895°	1.011e-14

Table 3.3: Convergence of the solution of the system in nominal position for parallel configuration

As shown in Tables 3.3 and 3.4, this method used to evaluate the initial guess x_0 results in a residual norm of the order of 5–10. The Newton–Raphson iterations quickly

Perpendicular Configuration (nominal position)				
k	$\theta_{2,k}$	$\phi_{2,k}$	$\theta_{3,k}$	$\|F(x_k)\|$
0	182.4829°	5.7635°	357.6899°	6.497e+00
1	182.9230°	5.7315°	357.7001°	1.655e-01
2	182.9254°	5.7317°	357.7001°	8.838e-04
3	182.9254°	5.7317°	357.7001°	2.668e-08
4	182.9254°	5.7317°	357.7001°	3.639e-14

Table 3.4: Convergence of the solution of the system in nominal position for perpendicular configuration

refine this estimate, and the solution appears to reach the exact root already after the third step. However, the convergence check based on $\|F(x_k)\| < 10^{-12}$ prevents premature termination due to machine precision limitations. Figure 3.7 show the reconstructed spatial configurations of the mechanism in the nominal position for both the parallel and perpendicular rotary actuator cases. The two revolute joints are represented as cylindrical bodies to highlight the rigid rotation axes in points O and P, while the spherical joints at points A and B are marked by colored spheres.

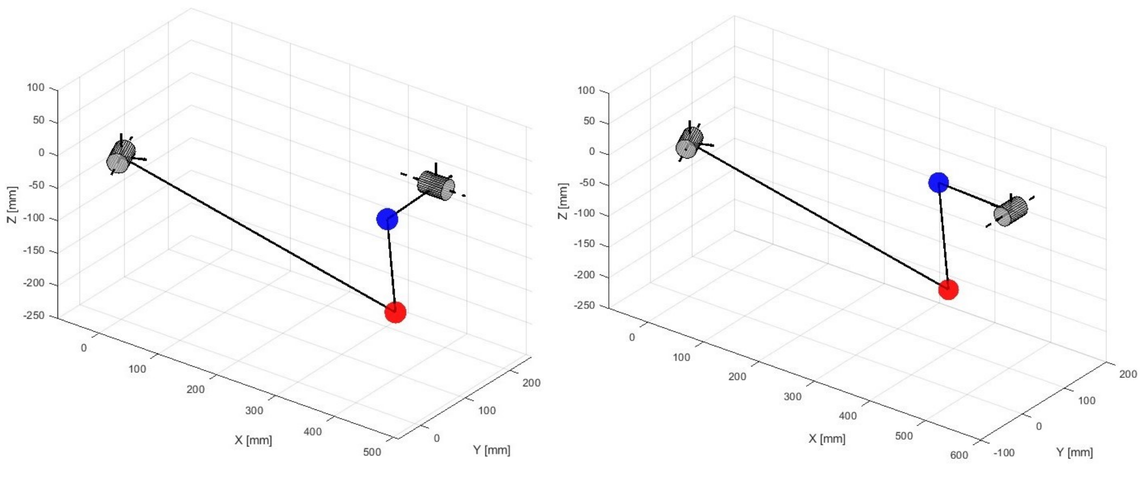

(a) (b)

Figure 3.7: Solution of the systems in nominal position: (a) parallel, (b) perpendicular

Following the methodology applied to solve the nominal position of the systems using the reference geometric values reported in Table 3.2, the same approach can now be extended to evaluate the kinematic behavior of the suspension-actuator system throughout the entire suspension stroke.

The nominal position of the system is defined by $\theta_{1,nom} = 0°$, thus defining the reference value for the trailing arm sweep. The positions assumed by point A along the full suspension stroke are obtained by applying Rodrigues' rotation matrix (see Equation 3.3) from the lower limit $\theta_{1,min} = -9.086°$ to the upper limit $\theta_{1,max} =$

9.683°. This procedure defines the boundary positions $A_{min} = A(\theta_{1,min})$ and $A_{max} = A(\theta_{1,max})$, given as input to the system.

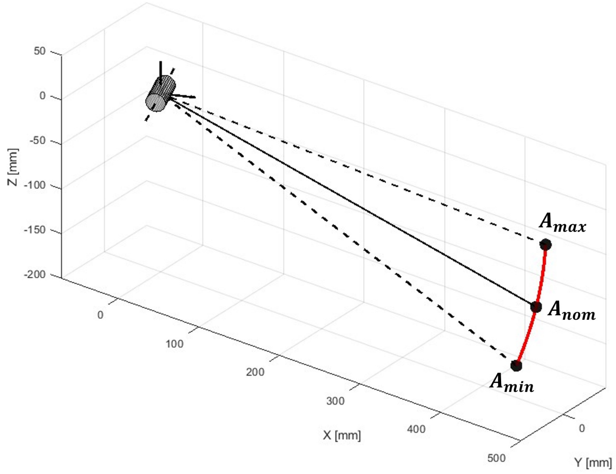

Figure 3.8: Point A full sweep from A_{min} to A_{max}

For a fixed system configuration, defined by the combination of L_2, L_3, P_x, P_y and P_z, the trailing arm motion is discretized over the range $[\theta_{1,\text{min}}, \theta_{1,\text{max}}]$. Then, for each discrete angle $\theta_{1,i} \in [\theta_{1,\text{min}}, \theta_{1,\text{max}}]$, the position of the point A is given by $A_i = A(\theta_{1,i})$. The kinematic problem is first solved at A_{min}. At this initial step, a coarse grid search is employed to determine a suitable initial guess $x_{0,1}$ for the Newton–Raphson first iteration. Once the first configuration is computed, the solution of the system $[\theta_{2,min}, \phi_{2,min}, \theta_{3,min}]^T$ is used as the initial guess for the subsequent position to be solved. This procedure is iterated up to the final position A_{max}, following the rule:

$$x_{0,(i+1)} = [\theta_{2,i}, \phi_{2,i}, \theta_{3,i}]^T \tag{3.18}$$

This strategy ensures solver convergence at every step and dramatically reduces the computational cost, since the coarse grid search is performed only once, rather than at each position of the system along the suspension stroke.

The methodology described in this section allows the kinematic configuration of the mechanism to be determined for any position of the trailing arm. This capability is essential for the subsequent optimization of the suspension-actuator system layout discussed in the next section.

3.3 Layout optimization of the system

Once the kinematic solution procedure has been established, the next step is to determine the optimal layout of the suspension-actuator system, defined by the combination of the link lengths L_2 and L_3, the position of point P, and the orientation of the rotary actuator shaft with respect to the vehicle longitudinal axis. The aim of the optimization is to improve the overall performance and efficiency of the system throughout the entire suspension stroke, while ensuring that all kinematic and geometric constraints are satisfied. To efficiently explore the design space and identify the best configuration of the system, a *multi-objective genetic algorithm* [19] is employed due to its effectiveness in handling complex multi-variable design problems.

The following sections describe the definition of the optimization problem, including the objectives and constraints, the implementation of the genetic algorithm, the analysis of the resulting solutions, and the selection of the final system configuration based on performance and feasibility criteria.

3.3.1 Definition of the problem and objectives

The functional and geometric requirements introduced in Sections 3.1.1 and 3.1.2 are translated into quantitative objectives and constraints for the optimization. The objectives establish the target performance of the suspension-actuator system and provide clear criteria to guide the search for the optimal layout. The first functional objective concerns the transmission ratio from the wheel hub to the gearbox input of the RRSA, denoted as τ_l. The target value of transmission ratio τ_{target} is defined in the nominal position of the suspension, corresponding to the equilibrium position around which the suspension oscillates and where the actuator operates most of the time. This value can be determined by evaluating the reference force that the actuator must satisfy at the wheel hub through several quarter-car simulation, in which the actuator is modeled using a Skyhook control logic:

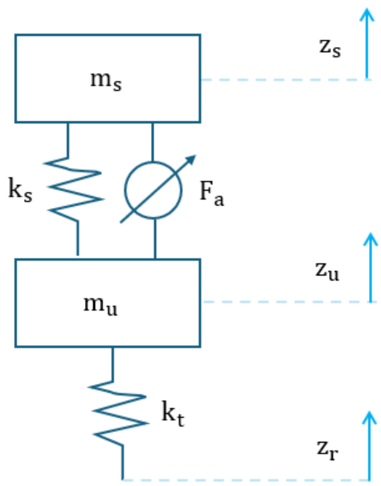

Figure 3.9: Quarter-car model with Skyhook control logic

In this model, the actuator force F_a is composed of two contributions: a standard suspension damper c_s acting between the sprung and unsprung masses, and an additional Skyhook damper c_{sky} that only reacts to the vertical velocity of the sprung muss. Unlike a classical Skyhook damper, which ideally acts between the vehicle body and a fixed “sky” reference [20], in this implementation c_{sky} applies a force to both sprung and unsprung masses, according to:

$$F_a = -c_s\,(\dot{z}_s - \dot{z}_u) - c_{sky}\,\dot{z}_s \tag{3.19}$$

Two quarter-car configurations were considered to explore two opposite suspension damping strategies: a comfort-oriented setup, characterized by lower damping values, and a handling-oriented setup, with increased damping to improve body motion control. In both configurations, the masses, the suspension spring stiffness and the tire stiffness are kept constant, while only the coefficients c_s and c_{sky} are varied. The parameter sets adopted for these two cases are reported in Table 3.5.

Quarter-car model data			
Vehicle parameter	**Description**	**Value**	**Unit**
m_s	Sprung mass	219.7	kg
m_u	Unsprung mass	43	kg
k_s	Suspension spring	22.2	kN/m
k_p	Tire stiffness	240	kN/m
Comfort configuration			
c_s	Suspension damper	1000	Ns/m
c_{sky}	Skyhook damper	10000	Ns/m
Handling configuration			
c_s	Suspension damper	2000	Ns/m
c_{sky}	Skyhook damper	5000	Ns/m

Table 3.5: Quarter-car model data: comfort vs handling configuration

The quarter-car model is excited using a sinusoidal bump input at the wheel, representing the passage of the vehicle over a localized road irregularity. This excitation provides a controlled and repeatable disturbance with a well-defined amplitude and duration, allowing the actuator–suspension interaction to be evaluated over a single compression–rebound event. Such excitation is well suited to identify peak suspension deflections, force transmission characteristics, and sprung and unsprung mass dynamics under transient conditions. The road bump profile $h(t)$ is implemented in the time domain as:

$$h(t) = \frac{h_0}{2}\left[1 - \cos\left(\frac{2\pi\, t}{L_b}\right)\right] \tag{3.20}$$

where h_0 is the bump maximum height, and L_b is the bump width. In the present work, the simulations considers a vehicle travelling at $70\,km/h$, taking a bump of height $h_0 = 2\,cm$ and width $L_b = 0.5\,m$:

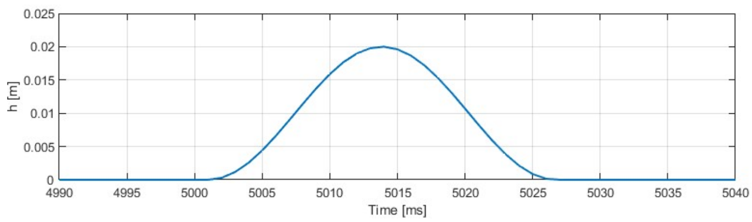

Figure 3.10: Synusoidal bump profile: $v_{vehicle} = 70\,km/h,\ h_0 = 2\,cm,\ L_b = 0.5\,m$

The simulation environment is implemented in MATLAB/Simulink and the overall scheme is illustrated in Figure 3.11. The model is divided into functional subsystems, including the sprung/unsprung mass dynamics, tyre-ground interaction, actuator force calculation and road profile generation. Gravity is applied to both masses to compute the static equilibrium position and to enable the occurrence of wheel hop, i.e. loss of tyre contact when $F_{tire} \leq 0$.

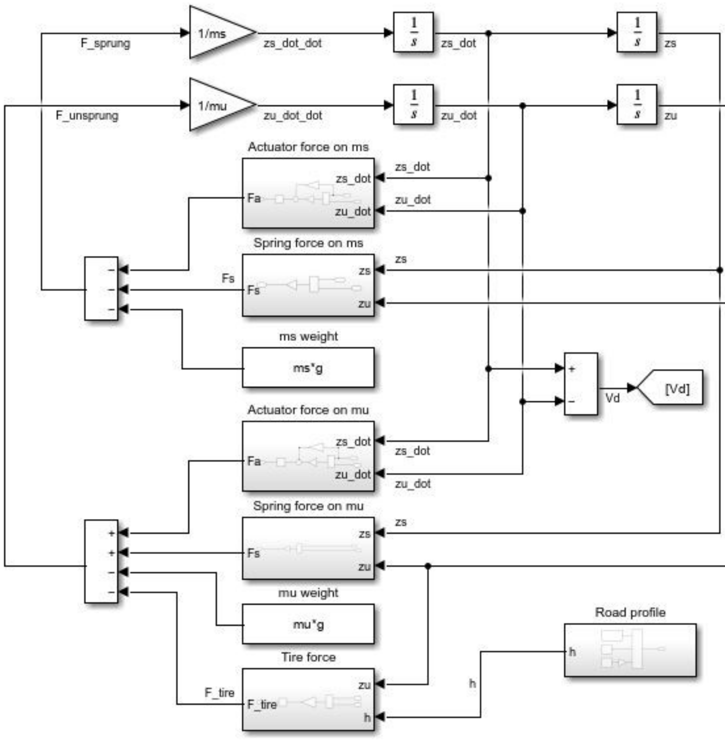

Figure 3.11: Quarter-car Simulink model

This approach allows identifying the target transmission ratio that the system must satisfy in the nominal suspension position, by limiting the maximum force that the actuator must deliver to the wheel hub, while preventing high actuator speeds that could produce back-EMF levels exceeding the limits of the power electronics.

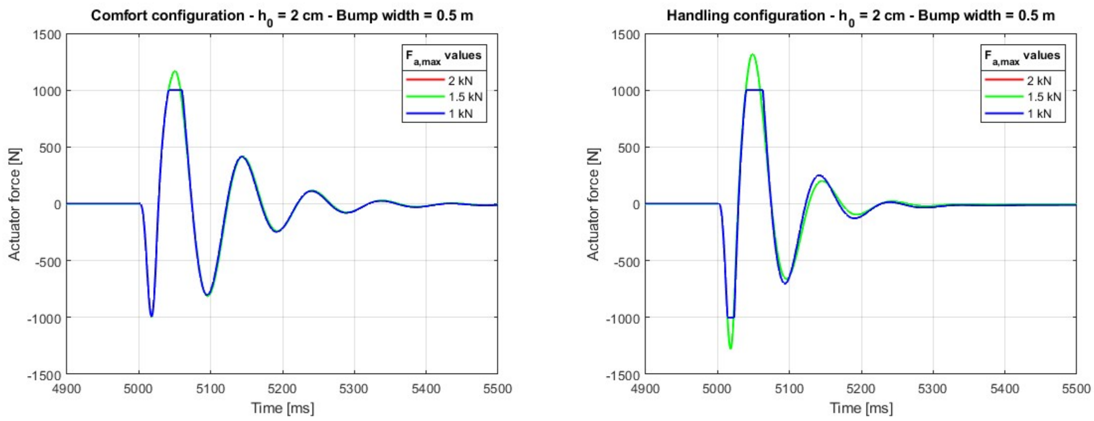

(a) (b)

Figure 3.12: Actuator force time history: (a) comfort, (b) handling

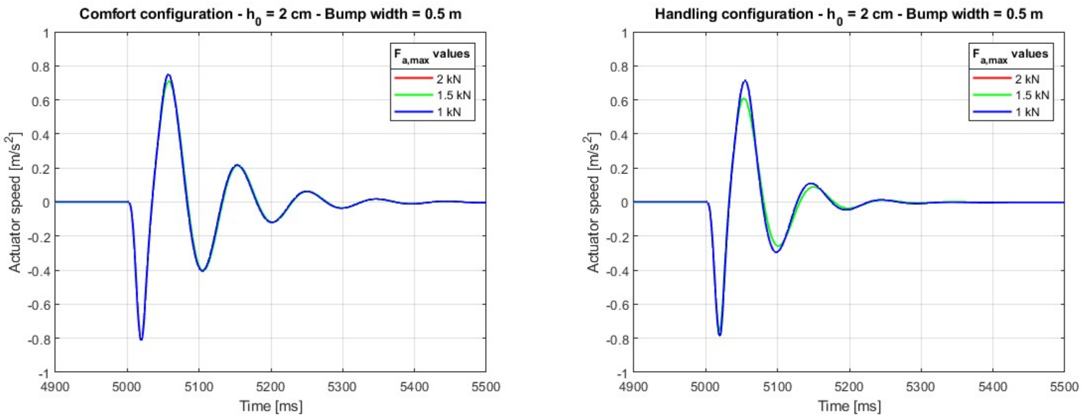

(a) (b)

Figure 3.13: Actuator force time history: (a) comfort, (b) handling

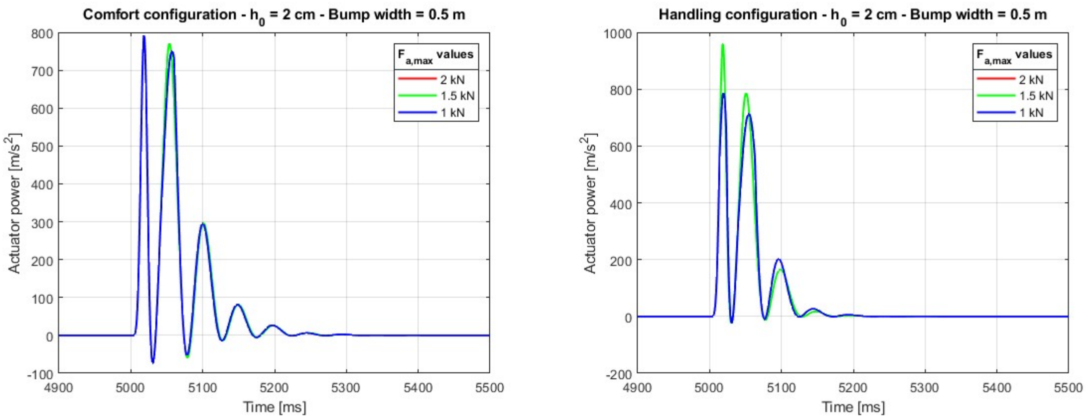

(a) (b)

Figure 3.14: Actuator power time history: (a) comfort, (b) handling

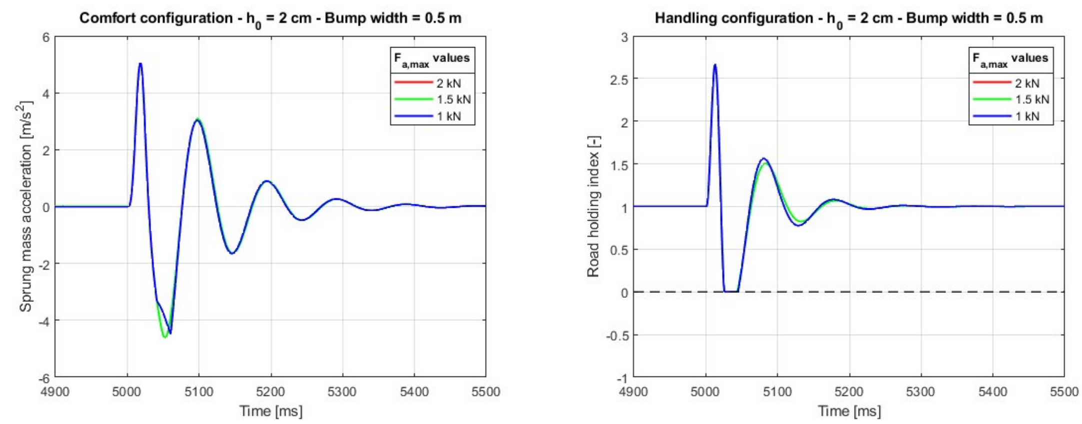

(a) (b)

Figure 3.15: Time histories of: Sprung mass acceleration in comfort (a) and Road holding index in handling (b)

In each simulation, the bump excitation is applied after a short settling time, allowing the system to reach its static equilibrium under the weight of the masses, corresponding to a constant tire force equal to $(m_s + m_u)g$. The maximum actuator force F_a was limited to 3 different values: $2\,kN, 1.5\,kN$ and $1\,kN$. When the actuator force is limited to $2\,kN$, the results are essentially the same as those obtained with $1.5\,kN$ and the red line is superimposed by the green one, since this force level is never reached during the simulation and therefore no saturation occurs. In this case, actuator saturation (visible in Figure 3.12) slightly alters the oscillations and peaks of other variables, as the force that cannot be delivered by the actuator is redistributed among the other components of the system. In terms of actuator speed, defined as the relative speed between unsprung and sprung masses (Figure 3.13), the results seem to be similar between comfort and handling configurations, with only a slight increase in the peak value when the actuator force is limited to $1\,kN$, thus slightly worsening the performances. In terms of actuator power (Figure 3.14), defined as $P_a = F_a\,v_a$, the peak values obviously decrease by limiting the actuator force to $1\,kN$, but even with $F_{a,max} = 1.5\,kN$, the actuator power remains well within the system constraint of $P_{a,max} = 1\,kW$. For the comfort configuration, the system performance is assessed through the sprung mass acceleration (Figure 3.15a). When $F_{a,max} = 1\,kN$, a slight discontinuity is observed during saturation, but the overall oscillatory behavior after the first peak remains unchanged. For the handling configuration, performance is evaluated using the road-holding index (Figure 3.15b), defined as the ratio between the instantaneous tire force and the static weight of the system:

$$\eta_{RH} = \frac{F_{tire}}{(m_s + m_u)g} \tag{3.21}$$

The index shows wheel detachment for a very short period, followed by small oscillations, with a similar trend by saturating the actuator force of both $1.5\,kN$ or $1\,kN$.

Based on the simulation results, a reference actuator force of $F_{a,ref} = 1.5\,kN$ at the wheel hub is selected to define the target transmission ratio τ_{target}. This value represents a suitable compromise: it keeps the actuator power within the limits of the power electronics, while allowing sufficiently high wheel-hub velocities to avoid excessive back-EMF generation. At the same time, it provides an adequate baseline rotational speed for the electric machine, enabling operation close to its optimal torque region and ensuring effective force transmission throughout the suspension stroke.

Feature	**Symbol**	**Value**	**Unit**
Phase-to-phase max voltage	V_{max}	60	V
Peak motor power	P_{max}	1	kW
Peak motor torque	$T_{em,max}$	1.9	Nm
Base motor speed	w_{base}	5200	rpm
Maximum motor speed	w_{max}	8900	rpm
Gearbox transmission ratio	τ_g	1:87.35	-

Table 3.6: New RRSA prototype specifications

For this application, the RRSA unit considered has different performance characteristics compared to the prototype introduced in Section 2.2.1, particularly in terms of maximum torque, maximum rotational speed and base speed of the electric machine, as reported in Table 3.6. From the reference wheel-hub force and the maximum actuator torque at gearbox output, the target transmission ratio in nominal suspension position can be directly computed as:

$$\tau_{target} = \frac{T_{em,max}}{\tau_g \, F_{a,ref}} \approx 111 \, \frac{mm}{rad} \tag{3.22}$$

The corresponding characteristic wheel-hub vertical speeds can be derived from the actuator rotational speeds, considering the kinematic relation:

$$v_{wh} = \frac{w_{em}}{\tau_{target} \, \tau_g} \tag{3.23}$$

By substituting the values of w_{base} and w_{max} into Equation 3.23, the corresponding wheel hub vertical speeds are found:

$$v_{wh,base} \approx 0.69 \, \frac{m}{s}; \qquad v_{wh,max} \approx 1.18 \, \frac{m}{s} \tag{3.24}$$

These two velocities assess whether the actuator can: (i) operate in the high-torque region during normal suspension motion, and (ii) reach sufficiently high speed without causing excessive back-EMF during peak transient events.

The second functional objective concerns the transmission angle of the linkage, denoted as γ. The target value is defined as $\gamma_{target} = 90°$ in the nominal position of the suspension. Values of γ close to 90° ensure an optimal mechanical advantage, allowing the actuator to transmit forces efficiently while minimizing the sensitivity of the mechanism to manufacturing tolerances, joint clearances, and thermal expansions. Conversely, angles approaching 0° or 180° can lead to self-locking of the mechanism, requiring excessively high actuator torque for small wheel hub loads. For this reason, the optimization seeks configurations that maintain the transmission angle within a practical range of $90° \pm 50°$ along the suspension travel [13, 14], thus improving force transmission and maintaining robust and stable operation throughout the stroke.

3.3.2 Specific design constraints

The geometric considerations introduced in Section 3.1.2 define the admissible spatial configuration of the RRSA and the linkage within the suspension architecture. For the present optimization problem, these geometric considerations are reformulated as explicit design constraints that restrict the feasible solution space and prevent configurations that would compromise packaging, kinematic integrity, or component mounting. These constraints are enforced at discrete suspension positions within the allowed vertical travel, ensuring that the RRSA and linkage remain operable and interference-free throughout the entire stroke.

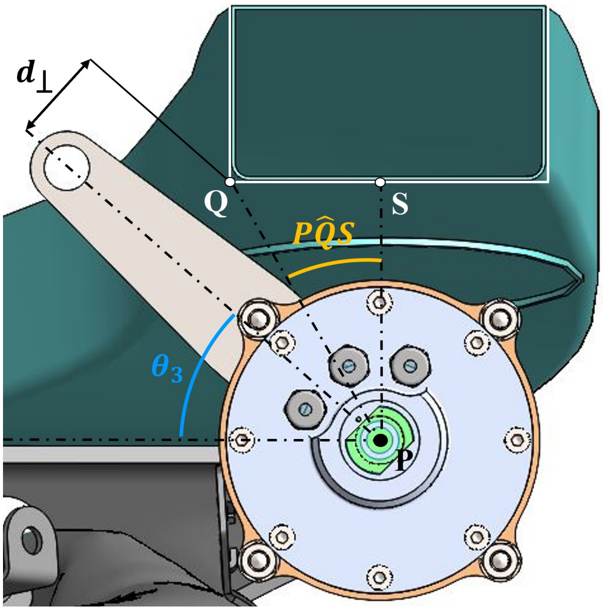

Figure 3.16: Parallel configuration: constraint about L_3 contact

The first constraint concerns the potential interference between the linkage levers and the longitudinal chassis member. In the parallel configuration, this issue primarily manifests when the push-rod attachment point A reaches the proximities of its maximum vertical position (see Figure 3.8), where lever L_3 moves closer to the chassis rail. In this situation, the possibility of contact between the lever L_3 and the chassis must be strictly avoided by defining a minimum distance requirement between them, as shown in Figure 3.16. The geometric condition is expressed by requiring that the minimum normal distance between the axis of the lever L_3 and the edge of the longitudinal chassis member at point Q remain greater than a prescribed safety clearance $d_{\perp,min}$, satisfying the condition:

$$d_\perp = |\vec{PQ}| \sin\left(90^\circ - \theta_3 - P\hat{Q}S\right) > d_{\perp,min} \tag{3.25}$$

In the perpendicular configuration, this problem is fully avoided, since the lever L_3 rotates in a plane parallel to the zx plane. In order to avoid interference between the lever and the longitudinal beam of the chassis the position of the point P must be limited in the y-direction with an upper limit $P_{y,max}$.

The second constraint concerns the potential interference between the push-rod–lever joint B and the wheel assembly, including both the rim and the tire envelope. Due to the lateral and vertical motion induced by suspension travel, point B progressively approaches the rotating assembly, which represents a strict no-go region that cannot be penetrated. This clearance requirement is particularly relevant in the parallel configuration, where B lies closer to the wheel and undergoes a larger y-displacement within the wheel envelope during suspension motion, requiring a lower limit $B_{y,min}$. In the perpendicular configuration, instead, the requirement is inherently satisfied by the placement of point P. To simplify, the limits of B in y-direction becomes the limits of P in y-direction for the perpendicular configuration, as depicted in Figure 3.17.

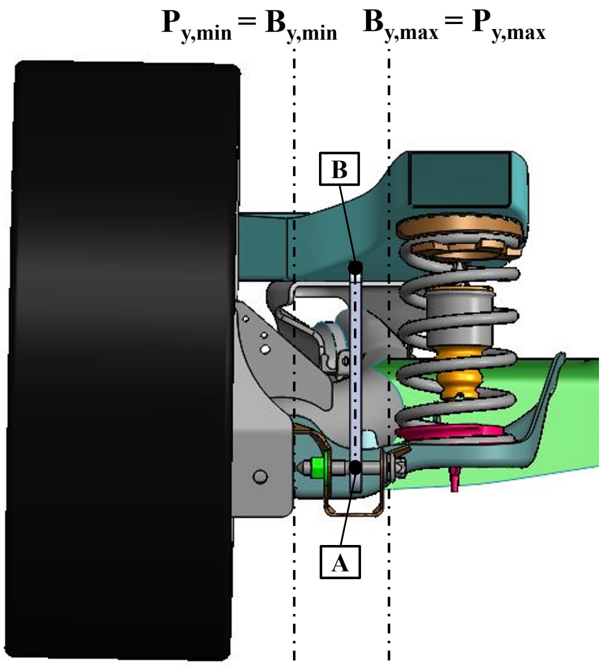

Figure 3.17: Rim and wheel envelope constraint

A further aspect to be considered concerns the admissible positions of point P (and therefore of the RRSA itself) along the x direction. In particular, a minimum allowable coordinate $P_{x,\min}$ must be imposed to prevent interference between the rotary actuator and the coil spring assembly. As shown in Figure 3.18, the output shaft of the RRSA protrudes several centimeters from the gearbox casing, which reduces the available space between the actuator and the spring seat.

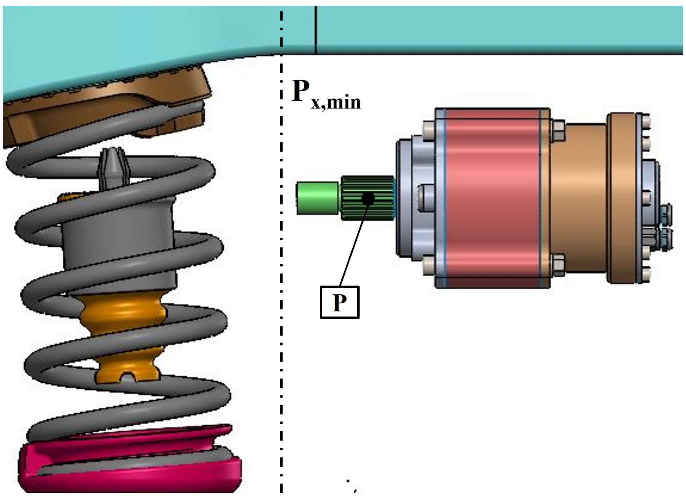

Figure 3.18: Spring assembly envelope constraint

A further constraint concerns the admissible vertical positions of points B and P. A maximum vertical limit $B_{z,\max}$ is imposed for the joint between the lever-arm and the push-rod in order to avoid interference with the wheelhouse components and with the upper chassis structures. Conversely, both upper and lower vertical bounds $P_{z,\max}$ and $P_{z,\min}$ are introduced for the RRSA hinge point to prevent contact between the actuator envelope and the longitudinal chassis rail, while also avoiding the risk of ground interference during full rebound.

The formalization of these geometric constraints is essential for the subsequent optimization stage. By expressing each of them as inequality conditions over the admissible suspension stroke, the design space is rigorously restricted to physically feasible and kinematically consistent configurations. This prevents the genetic algorithm from exploring solutions that, although mathematically valid, would be unachievable due to packaging conflicts or mounting limitations. As a result, the search domain is significantly reduced, improving convergence efficiency and ensuring that the optimal layouts identified by the GA correspond to implementable RRSA and linkage arrangements.

3.3.3 Genetic algorithm optimization

Genetic Algorithms (GAs) represent a class of stochastic optimization methods inspired by the mechanisms of natural evolution [19]. In this framework, a population of candidate solutions evolves through generations under the action of *selection*, *crossover*, and *mutation* operators. Individuals are evaluated through a *fitness function*, and those exhibiting higher performance are statistically more likely to propagate their characteristics to subsequent generations. Over iterations, the population tends to converge toward solutions that maximize or minimize the fitness objective, enabling the algorithm to efficiently explore complex multidimensional search spaces. In the present work, the multi-objective optimization is implemented using the Matlab built-in function *gamultiobj*, which is constructed according to a *Non-Dominated Sorting Genetic Algorithm II* [21]. *NSGA-II* is a controlled elitist genetic algorithm that balances convergence toward the Pareto front with population diversity. In a multi-objective optimization context, the Pareto front represents the set of solutions for which no objective can be improved without degrading at least one other objective. In other words, the points that appears on the Pareto front (best individuals) are *non-dominated solutions*, and define the trade-off between competing objectives, such as minimizing the deviation from the target transmission ratio in nominal position while minimizing deviations from the desired transmission angle of 90°. The algorithm assigns a rank to each individual based on dominance: individuals that are not dominated by any other solution belong to rank 1, those dominated only by rank 1 individuals belong to rank 2, and so on. Individuals with a lower rank have a higher probability of being selected as parents for the next generation. To preserve diversity along the Pareto front, crowding distance is computed for individuals of the same rank. This metric measures the separation between a solution and its neighbors in the objective space. Individuals with higher crowding distance are preferred during selection, as they help maintain a well-distributed set of Pareto-optimal solutions.

This optimization process evolves through a population of candidate solutions, also known as individuals, over successive generations. The process begins with an initial generation, which can be generated randomly or using a predefined distribution within the admissible design space. The choice of this initial population is crucial, as it directly influences the diversity of the search space and the ability of the algorithm to avoid premature convergence to suboptimal regions. Each generation consists of evaluating the current population according to the objective functions, followed by the application of genetic operators to produce a new generation of solutions. The algorithm iterates through this evolutionary process until a stopping criterion is met, which can be defined either as a maximum number of generations or based on the spread of the Pareto front, ensuring convergence toward a well-distributed set of non-dominated solutions, as summarized in Figure 3.19.

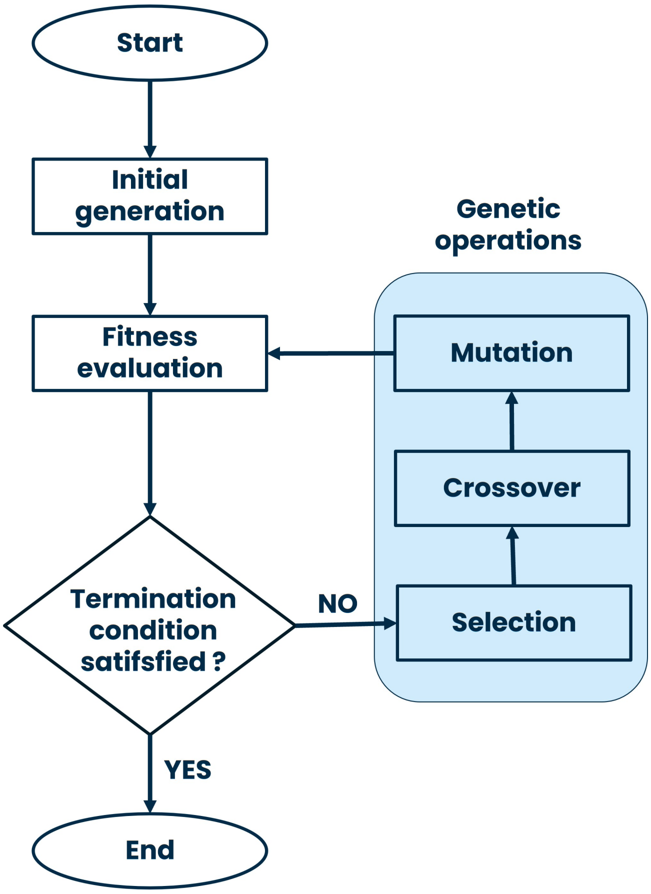

Figure 3.19: Genetic algorithm flow chart

Where the genetic operations are described as follows:

- **Selection**: Parents are chosen from the preceding generation using a combination of rank and crowding distance, favoring non-dominated solutions that are well spread along the Pareto front.

- **Crossover**: New solutions are created by mixing the traits of two parent solutions, producing individuals that inherit characteristics from both. This allows the algorithm to explore new regions of the design space while keeping the beneficial features from the parents.

- **Mutation**: Small random changes are applied to some solutions, introducing diversity in the population. This prevents the algorithm from getting stuck in suboptimal solutions and allows it to investigate unexplored regions of the design space.

In the optimization of the packaging of the linkage–RRSA system within the vehicle's twist-beam suspension, each individual is represented by a combination of five design variables, corresponding to the genes of the individual: the push-rod length L_2, the lever-arm length L_3, and the coordinates of the RRSA hinge point $P = [P_x,\ P_y,\ P_z]$. The set of these variables defines an individual (or genome) in the design space, expressed as:

$$g = [L_2,\ L_3,\ P_x,\ P_y,\ P_z] \tag{3.26}$$

Where each variable can take integer values expressed in millimetres within its respective *lower* and *upper bounds*, defined as inputs for the genetic algorithm:

$$\begin{aligned} l_b &= [L_{2,min},\ L_{3,min},\ P_{x,min},\ P_{y,min},\ P_{z,min}] \\ u_b &= [L_{2,max},\ L_{3,max},\ P_{x,max},\ P_{y,max},\ P_{z,max}] \end{aligned} \tag{3.27}$$

To ensure a complete exploration of the design space and to avoid premature convergence to suboptimal regions, the domain of possible solutions is initially mapped using a multidimensional grid created by discretizing each variable within its admissible bounds l_b and u_b. Considering a coarse discretization of each variable in 3 values - such as lower bound, middle value, and upper bound - the total number of potential individuals grows exponentially according to:

$$N_{individuals} = \left(n_{discretization\ levels}\right)^{N_{variables}} \tag{3.28}$$

For example, with five design variables and only three discretization levels per variable, the total number of different individuals becomes: $3^5 = 243$. Since every combination of variables must be evaluated by the fitness function (see Figure 3.19), a purely uniform discretization rapidly leads to a substantial computational burden as the resolution increases. Obviously, a coarse discretization with only 3 levels per variable could still lead to suboptimal solutions. Thus, To reduce the total number of evaluations while still ensuring an effective coverage of the design space, the discretization is constructed incrementally. The process starts from a minimum discretization level of three points per variable and progressively increases the resolution until a predefined grid size is reached. Variables are refined in descending order of their admissible range $(u_b - l_b)$, meaning that those exhibiting a wider interval are first assigned for additional discretization levels. This strategy prioritizes variables for which more intermediate values may significantly affect the solution, thus improving the likelihood of locating optimal regions within the admissible domain. Once the multidimensional grid is constructed, a subset of its points is used as the initial population for the genetic algorithm, ensuring that the first generation spans the domain uniformly before the evolutionary process begins. In this formulation, the total number of individuals resulting from the discretization is given by:

$$N_{individuals} = n_{L_2} \cdot n_{L_3} \cdot n_{P_x} \cdot n_{P_y} \cdot n_{P_z} \tag{3.29}$$

where n denotes the number of discretization levels assigned to each variable within their admissible limits. On the basis of the defined design variables, bounds, and constraints, the optimization problem can be formally stated as a constrained multi-objective minimization problem:

$$\min_{g \in \Omega} \mathcal{F}(g, \dots) = \begin{bmatrix} f_1(g) \\ f_2(g) \end{bmatrix} \tag{3.30}$$

where $\Omega \subset \mathbb{Z}^5$ denotes the admissible design space defined by the lower and upper bounds l_b and u_b. The minimization is intended in the Pareto sense: the genetic algorithm does not return a single optimal value of the objective vector, but a set of non-dominated individuals whose objective vectors are evaluated through a dedicated fitness function $\mathcal{F}(\cdot)$ that computes the objective values to be minimized while enforcing all geometric and kinematic constraints defined for each system configuration:

$$\big[\, f_1,\ f_2 \,\big] = \mathcal{F}\big(\, g,\ A_{swing},\ C_{system},\ K_{system} \,\big) \tag{3.31}$$

Here, A_{swing} contains the full trajectory of the point A from A_{min} to A_{max}. C_{system} is a discrete variable that specifies the RRSA configuration (parallel or perpendicular), while K_{system} collects all the kinematic and geometric constraints defined in Sections 3.3.1 and 3.3.2:

$$K_{system} = \big[\, B_{y,min},\ B_{y,max},\ B_{z,max},\ d_{\perp,min},\ \gamma_{max},\ \gamma_{min} \,\big] \tag{3.32}$$

For each candidate individual g, the kinematic chain described in Section 3.2.1 is solved to compute the positions assumed by the mechanism throughout the suspension stroke, including all the positions assumed from the joint B, the transmission ratio τ_l and the transmission angle γ. Then, the objectives can be computed from the knowledge of these quantities in the nominal position of the suspension:

$$f_1 = \left| \frac{\tau_{target} - \tau_{nom}}{\tau_{target}} \right|; \qquad f_2 = \left| \gamma_{target} - \gamma_{nom} \right| \tag{3.33}$$

where f_1 defines the normalized deviation of the nominal transmission ratio from the target value calculated in Section 3.3.1, while f_2 defines the deviation of the nominal transmission angle from the desired value of 90°.

Within the evaluation process for a single candidate individual g, if at any point along the suspension travel even a single system constraint contained in K_{system} is violated, the computation of the subsequent kinematic states of the system is stopped to reduce computational time. Instead of completing the full sweep described by A_{sweep}, the fitness function immediately returns a penalized objective value equal to 10^6 for both f_1 and f_2. The same penalization strategy is also applied whenever, at any configuration along the sweep, the Jacobian matrix employed in the iterative solution of the kinematic chain via the Newton–Raphson method becomes singular or nearly singular, compromising the numerical stability and convergence of the algorithm and indicating an inherently problematic or physically infeasible configuration of the mechanism, as described in Section 3.2.2. In such cases, the evaluation is interrupted and the individual is assigned the same penalized objective values. In this way, the corresponding solution is assigned a poor dominance rank and is therefore automatically discarded by the genetic algorithm. This mechanism allows the search to effectively avoid unfeasible regions of the design space and accelerates the identification of promising areas of the Pareto optimal frontier. After the evaluation of the initial population, the size of the subsequent generations is halved if at list half of the population leads to objective values different from 10^6, preserving feasible and non-dominated solutions while discarding dominated individuals and solutions that violate system constraints. This process is repeated until the population size reaches a predefined limit size imposed by the optimization setup.

Once the termination conditions are satisfied, the genetic algorithm is stopped, having progressively refined the population toward a set of feasible, non-dominated solutions that satisfy all imposed geometric and kinematic constraints. The resulting population constitutes the output of the optimization process and forms the basis for the analysis presented in the following section, where the characteristics and performance of the obtained solutions are discussed in detail.

3.3.4 Optimization results

After defining the main operations and workflow of the genetic algorithm, the next step is to set the specific numerical values required to initialize the optimization process. For each RRSA configuration, the admissible design space Ω is defined by specifying the lower and upper bounds l_b and u_b of the individual $g \in \Omega \subset \mathbb{Z}^5$, as defined in Eq. 3.27. The numerical values of these quantities adopted for each optimization are reported below:

Parallel Configuration		
Variable	$\boldsymbol{l_b}$ **[mm]**	$\boldsymbol{u_b}$ **[mm]**
L_2	120	130
L_3	140	160
P_x	430	480
P_y	80	140
P_z	40	60
Perpendicular Configuration		
Variable	$\boldsymbol{l_b}$ **[mm]**	$\boldsymbol{u_b}$ **[mm]**
L_2	150	200
L_3	110	160
P_x	570	610
P_y	-10	30
P_z	70	90

Table 3.7: Parallel configuration optimization setup

The matrix K_{system}, containing the kinematic and geometric constraints necessary to ensure the physical feasibility of the solutions within the design space, is the same for both configurations, since the remaining constraints on the position of point P are already embedded in the domain limits of the design variables:

Kinematic and geometric constraints		
Constraint	**Value**	**Unit**
$B_{y,min}$	-10	mm
$B_{y,max}$	30	mm
$B_{z,max}$	190	mm
$d_{\perp,max}$	30	mm
γ_{max}	40	deg
γ_{min}	140	deg

Table 3.8: Kinematic and geometric constrains optimization setup

The optimization results obtained for the two RRSA configurations are presented in terms of the Pareto-optimal solutions returned by the genetic algorithm:

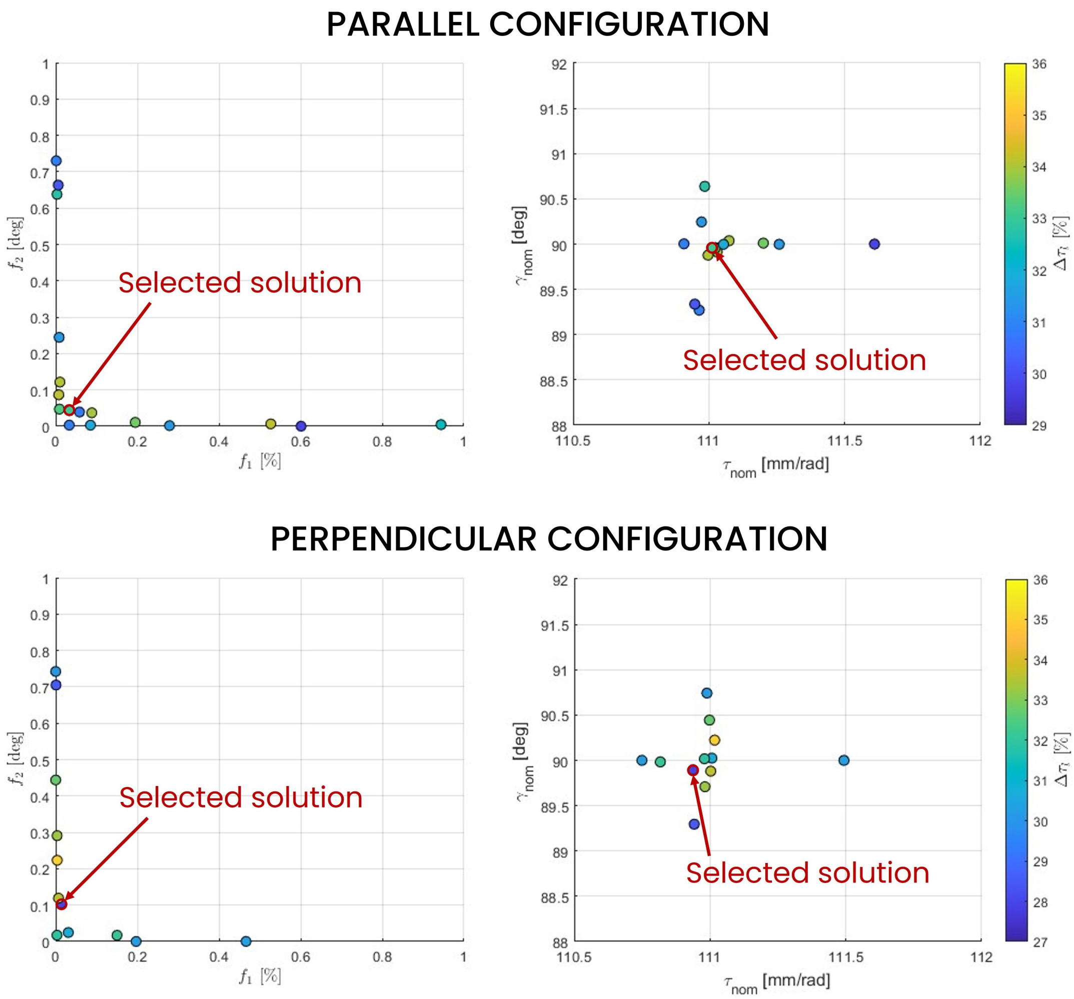

Figure 3.20: Pareto front optimization results for parallel and perpendicular configurations

The Pareto-optimal solutions reported in the left graphs of Figure 3.20 are concentrated in a region where both the percentage deviation of the nominal transmission ratio from the target value and the deviation of the nominal transmission angle from the desired value of 90° are relatively small. This confirms the ability of the genetic algorithm to efficiently explore the admissible design space and to converge toward an optimal set of solutions that satisfy all the imposed constraints. The distribution of optimal solutions clearly highlights the trade-off between the two objectives: solutions that achieve a transmission ratio very close to the target value may exhibit a larger deviation of the transmission angle from 90°, while solutions characterized by a nearly optimal transmission angle tend to show a higher deviation in the transmission ratio. As a consequence, no single solution can be considered optimal with respect to both objectives simultaneously, and the final design choice necessarily involves a compromise between these competing requirements. A more direct interpretation of the results is obtained by representing the Pareto-optimal solutions in terms of τ_{nom} and γ_{nom} values, as reported in the right graphs of Figure 3.20. In this representation, each solution is color-coded according to the maximum percentage deviation of the transmission ratio $\Delta\tau_l$ over the entire suspension travel with respect to its nominal value. From this perspective, it can be seen that some solutions exhibit a relatively low variation of the transmission ratio along the suspension travel, with maximum deviations of approximately $27 - 30\%$ with respect to the nominal value, as highlighted by the blue-colored points in the figure. However, despite this advantage, they do not necessarily guarantee that the nominal transmission ratio coincides with the target value defined for the system, leading to different values of force and velocity capabilities with respect to the ones defined by τ_{target} in Section 3.3.1. For this reason, the final selection of candidate solutions is based on a balanced trade-off between the proximity of the nominal transmission ratio to its target value, the proximity of the nominal transmission angle to 90°, and an acceptable level of percentage deviation of the transmission ratio along the suspension travel. The selected solutions and objectives are reported in the following tables:

Optimization solutions: individuals					
Configuration	$\boldsymbol{L_2}$	$\boldsymbol{L_3}$	$\boldsymbol{P_x}$	$\boldsymbol{P_y}$	$\boldsymbol{P_z}$
Parallel	123	148	446	139	44
Perpendicular	167	153	608	5	79

Table 3.9: Optimization solution: individuals

Optimization solutions: objectives					
Configuration	$\boldsymbol{f_1}$ [%]	$\boldsymbol{f_2}$ [°]	$\boldsymbol{\tau_{nom}}$ $\left[\frac{mm}{rad}\right]$	$\boldsymbol{\gamma_{nom}}$ [°]	$\boldsymbol{\Delta\tau_l}$ [%]
Parallel	0.02	0.04	111.02	89.96	≈ 31
Perpendicular	0.05	0.10	110.94	89.90	≈ 27

Table 3.10: Optimization solution: objectives

For each selected solution, the resulting trends of the transmission ratio τ_l and the transmission angle γ throughout the entire suspension travel are reported in Figure 3.21, providing a direct visualization of their variation along the wheel stroke.

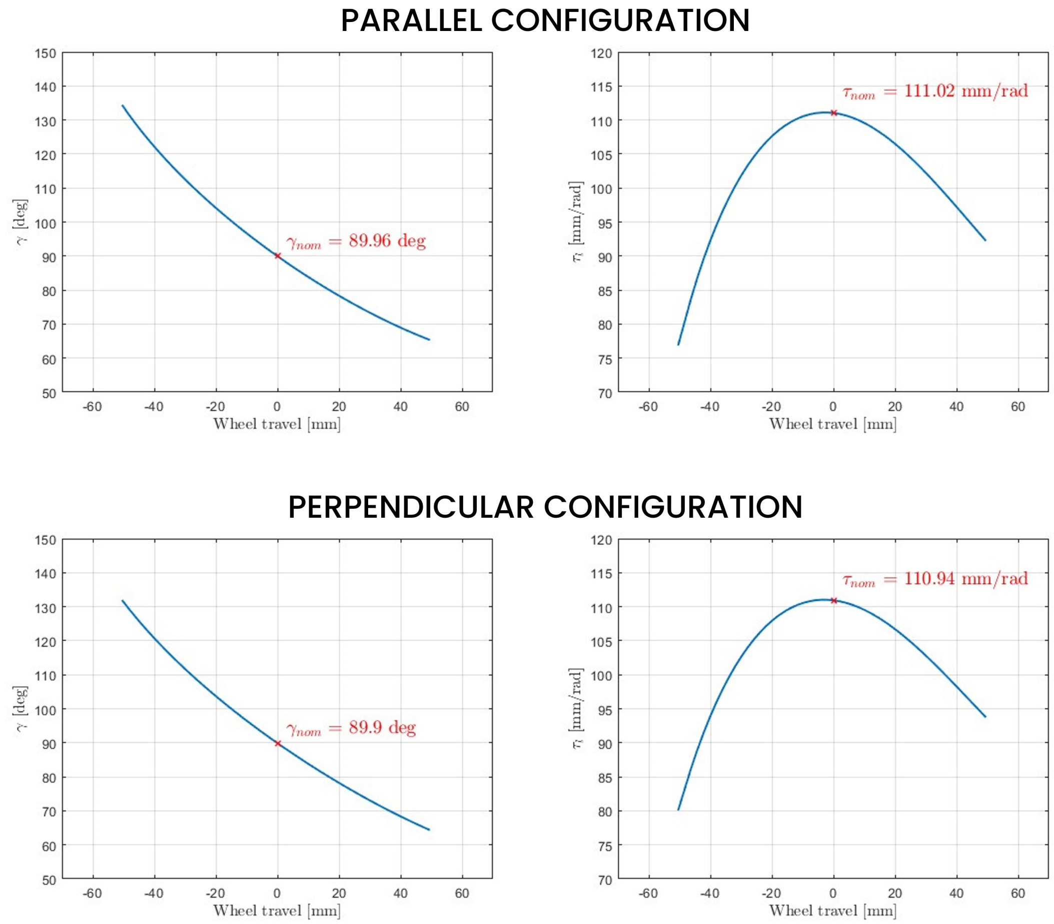

Figure 3.21: Transmission ratio and transmission angle trends along the suspension stroke of the selected solutions

These trends allow the most relevant results to be identified in terms of extreme values occurring at the maximum rebound and compression positions of the suspension defined by A_{min} and A_{max} for both configurations:

Extreme values of τ_l and γ along the suspension travel				
Configuration	γ_{min} [°]	γ_{max} [°]	$\tau_l(\gamma_{\min})$ $\left[\frac{mm}{rad}\right]$	$\tau_l(\gamma_{\max})$ $\left[\frac{mm}{rad}\right]$
Parallel	65.33	134.39	76.84	92.23
Perpendicular	64.34	131.93	80.04	93.74

Table 3.11: Extreme values of τ_l and γ along the suspension travel

Despite the slightly higher deviation of the nominal transmission ratio from the target value, the perpendicular configuration selected from the Pareto front in Figure 3.20 results in a lower maximum variability of the transmission ratio $\Delta\tau_l$ of approximately 27 %, compared to the parallel solution which reaches about 31 %, as reported in Table 3.10. At the same time, the perpendicular solution ensures a lower maximum transmission angle γ_{max} at the maximum suspension extension and a slightly lower minimum transmission angle γ_{min} at maximum suspension compression, with respect to the parallel configuration.

Overall, the comparative analysis of the optimization results highlights that, based on the considered performance indicators, the perpendicular RRSA configuration exhibits a more favorable balance between performances and robustness along the suspension travel. For this reason, it appears to be the most promising solution at this stage of the study. Nevertheless, the final choice cannot be based solely on the static and kinematic metrics discussed so far. Additional aspects related to the dynamic behavior of the mechanism for both configurations are therefore examined in the following section, in order to support a well-founded and consistent selection of the most suitable layout.

3.3.5 Selection of the final configuration

Beyond the kinematic performance assessed in Section 3.3.4, additional design aspects must be considered to support the final selection of the RRSA configuration. In particular, the feasibility of the optimized solutions must be verified with respect to the operating limits of the mechanical components adopted in the system, focusing on the relative angular excursions of the joints A and B, in order to ensure the correct functioning of the selected rod ends to be integrated into the push-rod assembly. In this work, *spherical plain bearing rod ends* are considered.

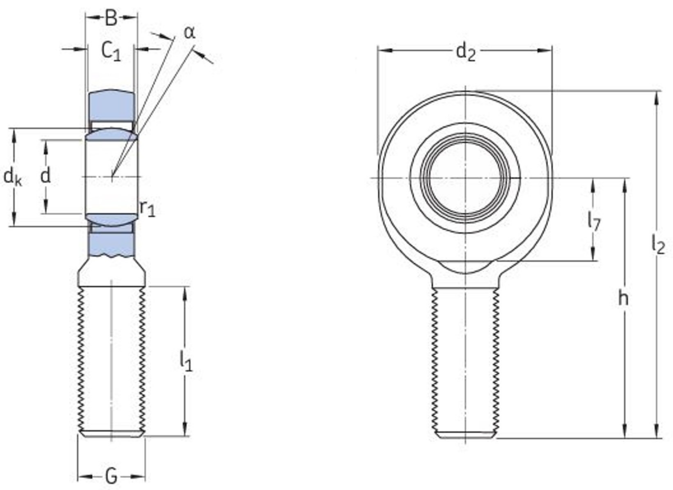

Principal dimensions						Angle of tilt	Basic load ratings dynamic	static	Mass	Designations Rod end with right-hand thread
d	d_2 max	G 6g	B	C_1 max	h	α	C	C_0		
mm						degrees	kN		kg	–
10	30	M 10	9	7,5	48	12	8,15	18,3	0,053	**SA 10 E**[1)]

Figure 3.22: Rod end SA10-E specifications [22]

These components consist of a housing with an integral shank that forms a seat for a spherical plain bearing, allowing relative angular motion while supporting predominantly radial loads and moderate axial forces. The SA 10 E rod end reported in Figure 3.22 is selected for the present application, based on the required M10 bore diameter of the push-rod connections and its suitability for the expected load and kinematic conditions. This type of rod end is commonly employed in linkage mechanisms where compactness, angular compliance, and load-carrying capability are required. Operating a rod end beyond its specified *angular misalignment* α can reduce the effective contact area between the bearing surfaces, increasing localized stresses and accelerating wear. Over time, this can result in material fatigue, increased clearances, and ultimately premature failure of the joint.

With the aim of assessing which configuration of the system provides a more favorable operating condition, the relative misalignment angles at joints A and B are evaluated for each configuration:

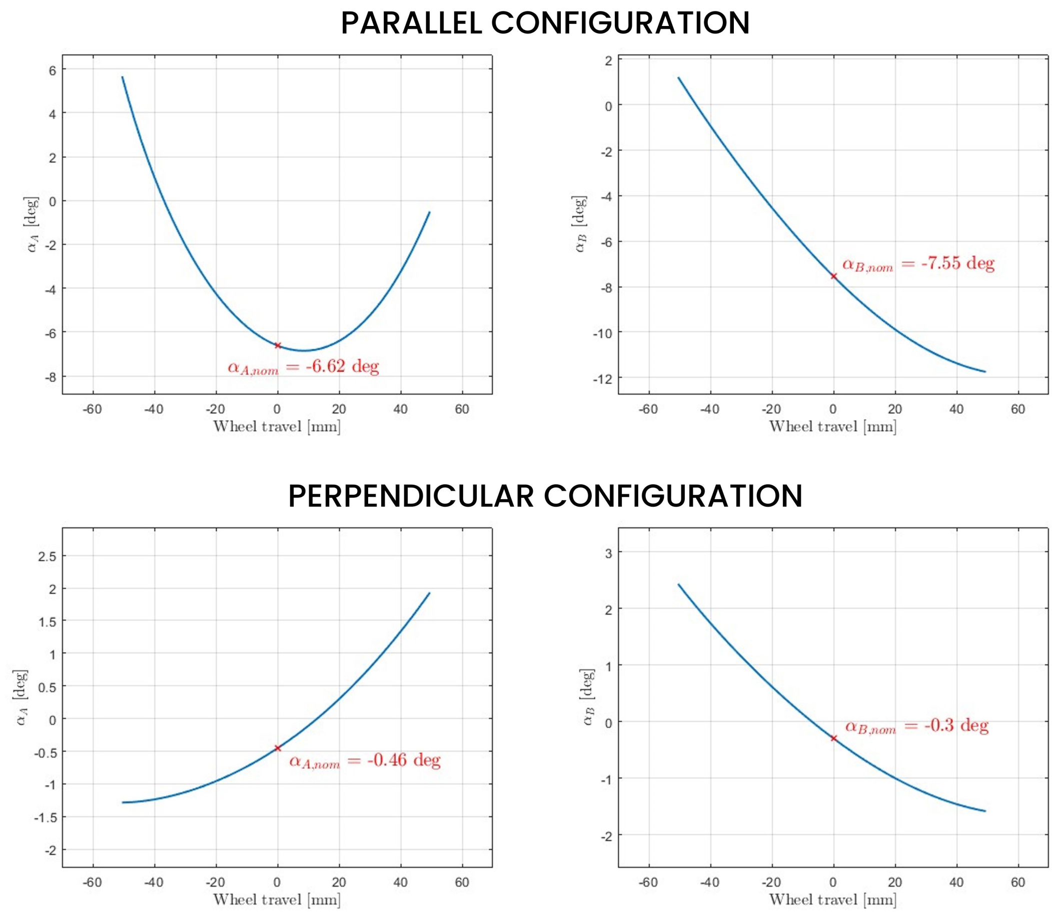

Figure 3.23: Push rod misalignment in joints A and B

In particular, the angles α_A and α_B are defined as the instantaneous angular deviations between the axis of the push rod and the corresponding bolt axis at joints A and B, respectively. The trends reported in Figure 3.23 highlight a marked difference between the two RRSA configurations. In the parallel configuration, joint B is required to undergo a relatively large displacement along the y-direction in order to follow the circular trajectory generated by the rotation of the lever about the vehicle longitudinal axis. This kinematic requirement results in significant variations of the misalignment angle at both joints A and B along the suspension travel. Moreover, the misalignment angles already assume relatively high values at the nominal operating position of the system, which represents an unfavorable working condition, since the mechanism must be able to operate around this position for most of the time. Conversely, the perpendicular configuration exhibits a substantially reduced variation of the misalignment angle for both joints throughout the entire suspension stroke. In this case, the misalignment angles remain close to zero in the nominal configuration and increase only moderately toward the extreme positions of suspension compression and extension. This behavior results in a more favorable load distribution within the rod ends, which is expected to improve the long-term reliability of the joints.

Misalignment angles $\boldsymbol{\alpha_A}$ and $\boldsymbol{\alpha_B}$				
Configuration	$\lvert\boldsymbol{\alpha_{A,nom}}\rvert$ [°]	$\lvert\boldsymbol{\alpha_{B,nom}}\rvert$ [°]	$\lvert\boldsymbol{\alpha_{A,max}}\rvert$ [°]	$\lvert\boldsymbol{\alpha_{B,max}}\rvert$ [°]
Parallel	6.62	7.55	6.86	11.75
Perpendicular	0.46	0.30	1.93	2.43

Table 3.12: Misalignment angles α_A and α_B

Another aspect that must be taken into account concerns the dynamic advantages or disadvantages of the two systems in terms of equivalent mass of the linkage, considering only the contribution of the push rod L_2 and the lever L_3. To this end, the vertical displacement of the point A can be described by a single generalized coordinate z. Under the assumption that the suspension mechanism behaves as a single-degree-of-freedom system within the considered motion range, the total kinetic energy of the linkage can be expressed in quadratic form with respect to the generalized vertical velocity $\dot{z}$:

$$T = \frac{1}{2}\, M_{eq}(z)\, \dot{z}^2 \tag{3.34}$$

where $M_{eq}(z)$ represents the equivalent mass of the linkage between the points A and P, as a function of the vertical movement of the suspension. To determine $M_{eq}(z)$, the total kinetic energy of the system is first written as the sum of the translational and rotational contributions of all moving bodies composing the linkage:

$$T = \sum_i \left(\frac{1}{2}\, m_i\, v_{G_i}^2 \;+\; \frac{1}{2}\, I_i\, \omega_i^2 \right) \tag{3.35}$$

where m_i denotes the mass of the i-th body, v_{G_i} is the velocity of the center of mass of the same body, while I_i and ω_i are their moment of inertia and angular velocity with respect to the axis of rotation. For the purpose of this qualitative comparative analysis, the masses of the push rod and the lever are assumed to vary linearly with their respective lengths. Both components are modeled as hollow circular sections with constant cross-sectional properties. Under this assumption, the mass of each element is computed as:

$$m_i = \rho \, A \, L_i \tag{3.36}$$

where ρ is the material density, A is the cross-sectional area of the hollow section, and L_i is the length of each body. Once the mass of each link is defined, the moment of inertia of the push rod and the lever are respectively:

$$I_2 = \frac{1}{12} m_2 \, L_2^2 \qquad ; \qquad I_3 = \frac{1}{3} m_3 \, L_3^2 \tag{3.37}$$

Since the mechanism is fully described by the vertical displacement z, the velocity of each point of the system can be written as:

$$v_i = \frac{dr_i}{dz} \dot{z} \tag{3.38}$$

Similarly, the angular velocity of each body can be expressed as:

$$\omega_i = \frac{d\theta_i}{dz} \dot{z} \tag{3.39}$$

For the push rod, whose orientation is described by the unit vector $\hat{u}_2$ along its longitudinal axis, the angular velocity can be obtained from the time variation of itself by neglecting the component along its own longitudinal axis:

$$\omega_2 = \hat{u}_2 \times \frac{d\hat{u}_2}{dz} \dot{z} \tag{3.40}$$

Considering that the push rod is translating and rotating about its center of gravity, while the lever is rotating around an axis passing through its end, the equation 3.35 of the total kinetic energy can be rewritten for the case under study, and collecting the terms multiplying $\dot{z}$, the equivalent mass of the linkage can be written as the sum of the individual contributions:

$$M_{eq}(z) = m_2 \left\| \frac{dr_{G_2}}{dz} \right\|^2 + I_2 \left\| \hat{u}_2 \times \frac{d\hat{u}_2}{dz} \right\|^2 + I_3 \left\| \frac{d\theta_3}{dz} \right\|^2 \tag{3.41}$$

The expression reported in Eq. 3.41 can be solved for both parallel and perpendicular configurations of the system as a function of the same wheel travel, corresponding to an equal displacement z. Figure 3.24 shows the equivalent mass of each system normalized with respect to its nominal value in order to highlight its relative variation along the suspension stroke. In general, the equivalent mass trend follows an approximately inverse relationship with the transmission ratio τ_l. It can be observed that the perpendicular configuration exhibits a smaller variation of the equivalent mass from the nominal value along the suspension travel compared to the parallel configuration.

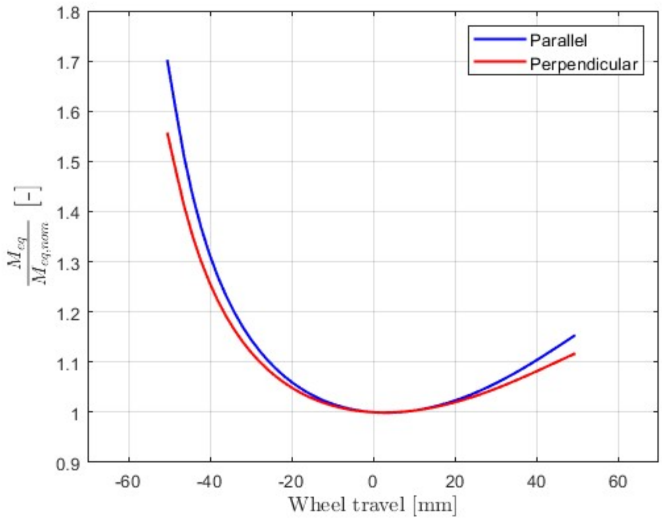

Figure 3.24: Normalized M_{eq} comparison between parallel and perpendicular configurations

This behavior is consistent with the higher angular velocity assumed by the push rod in the parallel layout. On the other hand, the higher push rod length in the perpendicular configuration leads to a higher nominal equivalent mass of the system, resulting in a generally higher inertial level over the suspension stroke.

Based on these considerations, even if it shows a worse dynamic response of the system due to the higher equivalent mass, the perpendicular configuration is identified as the most suitable solution due to the lower percentage deviation of transmission ratio and misalignment angles of the push rod along the entire suspension stroke, and is therefore selected as the final configuration of the system:

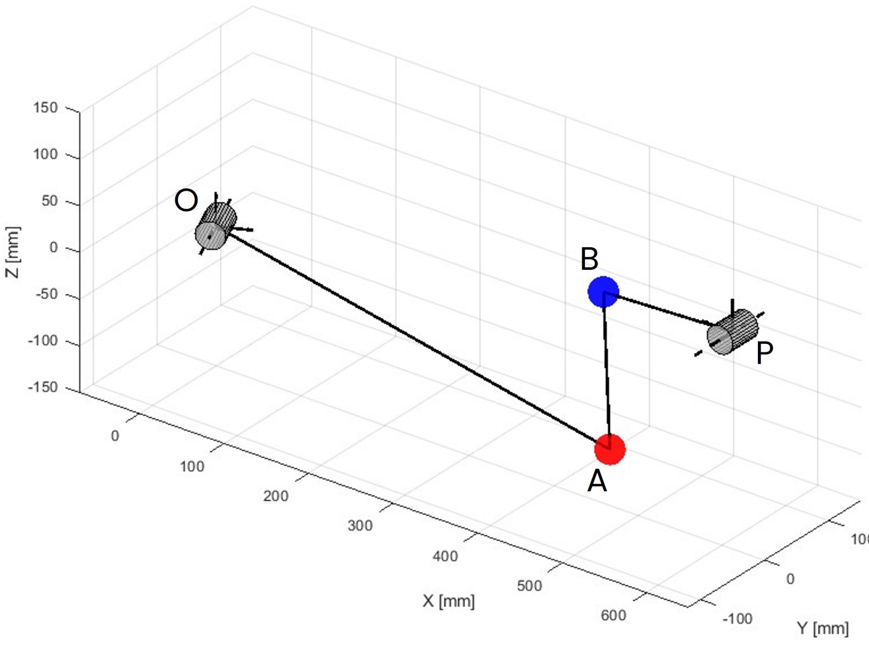

Figure 3.25: Final configuration solution of the system

Chapter 4

Mechanical linkage design

Once the perpendicular RRSA configuration has been identified as the most suitable solution, the design process proceeds with the detailed dimensioning of the linkage and the development of the corresponding CAD model. The aim of this chapter is to translate the optimized kinematic layout into a physically realizable mechanical assembly, ensuring structural integrity, manufacturability, and compatibility with the selected mechanical components.

The geometric dimensions of the lever and the push rod are defined based on the load cases derived from the suspension operation, while appropriate design criteria are chosen as a compromise between strength under service conditions and reduction of the equivalent mass of the system. The resulting geometry is then assembled together with the suspension components, leading to the definition of the complete system and its integration into the final assembly.

4.1 Load cases and force transmission

In order to proceed with the structural dimensioning of the linkage components, it is first necessary to identify the load cases acting on the system during operation. This section focuses on the evaluation of the forces transmitted through the lever and the push rod, starting from the actuation force generated by the electric motor under maximum torque conditions reported in Table 3.6, defined as:

$$F_{em,max} = \frac{T_{em,max}}{\tau_g \, L_3} \tag{4.1}$$

This force can be considered as a constant force applied at the end of the lever L_3 in joint B, and directed tangentially to the circular trajectory described by the lever rotation around point P. Then, the axial force acting on the push rod can be evaluated along the entire suspension travel through several steps. First, the force $F_{em,max}$ acting on the lever L_3 is decomposed as its component acting on the push-rod L_2 in the x-z plane as:

$$F_{push,xz} = \frac{F_{em,max}}{cos(\gamma')} \tag{4.2}$$

where γ' is defined as:

$$\gamma' = \gamma_{xz} - 90° \quad (4.3)$$

with γ_{xz} representing the projection of the transmission angle γ onto the x–z plane. The force $F_{push,xz}$ can then be decomposed into its components in the x-z plane two components in the x-z plane, identified by the angle $\phi_{2,xz}$:

$$\vec{F}_{push,xz} = F_{push,xz} \begin{bmatrix} \sin \phi_{2,xz} \\ 0 \\ \cos \phi_{2,xz} \end{bmatrix} \quad (4.4)$$

Finally, the axial force transmitted through the push rod is obtained by projecting $\vec{F}_{push,xz}$ along the direction of the push rod. This is performed through the scalar product between $\vec{F}_{push,xz}$ and the unit vector $\hat{u}_2$:

$$\left|F_{push}\right| = \vec{F}_{push,xz} \cdot \hat{u}2 \quad (4.5)$$

This force produces a pure tensile or compressive load state in the push rod L_2, depending on the suspension position. Conversely, the constant actuation force $F_{em,\max}$ acting at joint B generates a pure bending moment in the lever L_3 about point P. The trend of these forces along the suspension travel is reported below:

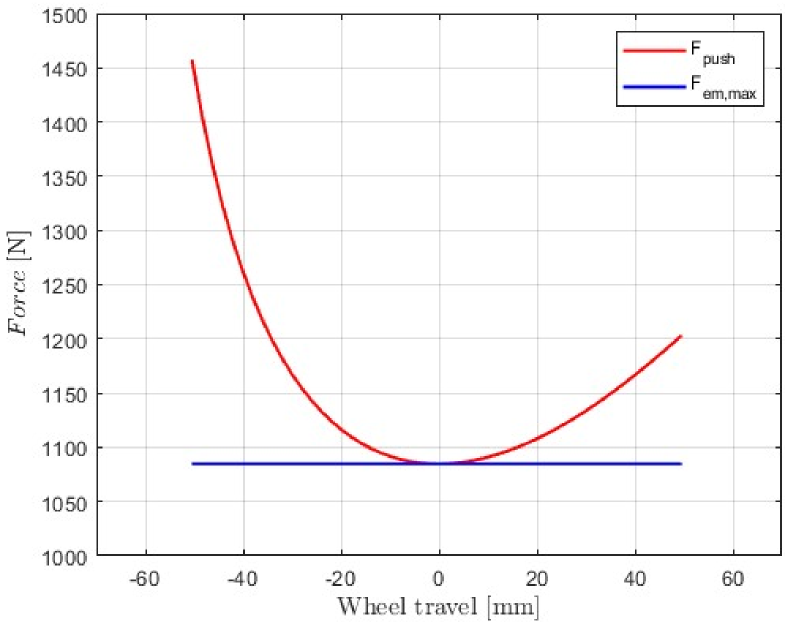

Figure 4.1: Push rod and lever force trends along suspension stroke

Since the transmission angle in the nominal suspension position is approximately equal to 90°, the force generated by the electric motor and transmitted through the lever L_3 is efficiently transferred to the push rod L_2, thus:

$$\left|F_{push,nom}\right| \approx F_{em,max} \approx 1090\, N \quad (4.6)$$

As the suspension moves away from the nominal configuration, the transmission angle progressively deviates from 90°. This results in a geometric amplification of the axial force F_{push}, which reaches its maximum values near the extreme positions of the suspension stroke. Since the transmitted mechanical power is ideally conserved, an increase in force amplification corresponds to an increase in the equivalent angular velocity at the motor shaft. Thus, an appropriate control strategy is needed to avoid an excessive level of back-EMF. However, the maximum value of F_{push} is reached when the suspension reaches its maximum extension position:

$$F_{push,max} = \left| F_{push}(\gamma_{\max}) \right| \approx 1460\, N \tag{4.7}$$

The force values retrieved can be used for the validation of the selected rod ends in terms of durability and free maintenance, and for lever and push rod dimensioning described in the next sections.

4.2 Rod ends validation

Once the maximum axial force transmitted through the push rod L_2 has been identified, the next step consists in verifying the suitability of the selected rod ends under the most severe operating conditions. Although the push rod is primarily subjected to axial loading, the spherical plain bearings installed at joints A and B may experience a combination of axial and radial loads due to the misalignment angles α_A and α_B arising from the three-dimensional kinematics of the suspension (see Figure 3.23).

Therefore, a proper decomposition of F_{push} along the local reference frame axis of each joint is required to assess their durability under service conditions:

$$\begin{cases} F_{A,r} = |F_{push}| \cos \alpha_A \\ F_{A,a} = |F_{push}| \sin \alpha_A \end{cases} \quad ; \quad \begin{cases} F_{B,r} = |F_{push}| \cos \alpha_B \\ F_{B,a} = |F_{push}| \sin \alpha_B \end{cases} \tag{4.8}$$

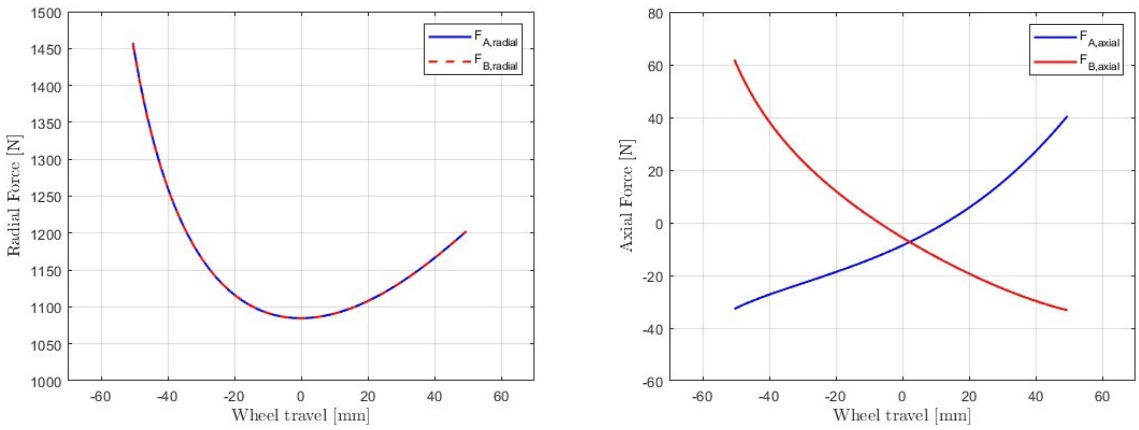

(a) (b)

Figure 4.2: Forces on A and B spherical plain bearings: (a) radial, (b) axial

As shown in Figure 4.2a, the radial load components acting on bearings A and B almost completely overlap throughout the suspension travel. Conversely, the axial components reported in Figure 4.2b exhibit an approximately opposite trend. This is a direct consequence of the spatial orientation of the rod ends, which leads to opposite projections of the push rod force along the local axial directions of the two bearings. These results allow the equivalent dynamic load acting on each rod end to be determined and subsequently compared with the manufacturer's specifications in order to verify the expected service life under the identified load case.

Forces acting on the joints A and B		
Joint	$\lvert \boldsymbol{F_{max,radial}} \rvert$ **[N]**	$\lvert \boldsymbol{F_{max,axial}} \rvert$ **[N]**
A	1455	35
B	1455	60

Table 4.1: Forces acting on the joints A and B

The maximum values of the radial and axial force components acting on each joint reported in Table 4.1 are used to evaluate the permissible load of the bearings [22], according to:

$$P_{perm} = C_0\, b_2\, b_6 \tag{4.9}$$

Where C_0 is the static load rating of the bearing reported in the table of Figure 3.22, b_2 is the temperature factor, assumed equal to 1 under ambient operating conditions, and b_6 depends on the type of load acting on the bearing:

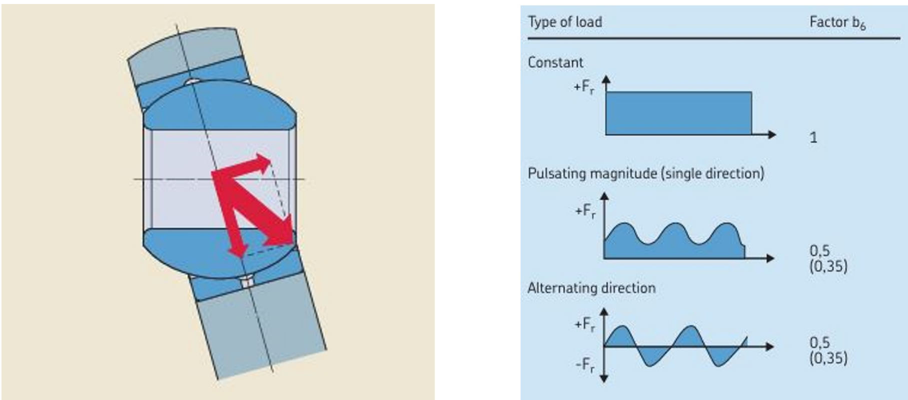

Figure 4.3: Rod ends permissible load evaluation [22]

Once the permissible load is calculated, the specific bearing load can be retrieved from:

$$p = K\,\frac{P_{perm}}{C} \tag{4.10}$$

Where K is the specific load factor, depending on the bearing design and sliding contact surface combination, assumed as $K = 50$ for steel/bronze contact surfaces, and C is the dynamic load factor reported in 3.22

Since the rod ends are validated in their worst operating conditions, the loads can be considered applied in alternating directions within a misalignment angle of $\beta \approx \pm 3°$ for each rod, at a certain frequency f, corresponding to a continuous alternating suspension motion from A_{min} to A_{max}. The mean sliding velocity can be then computed as:

$$v = 5.82 \cdot 10^{-7}\, d_m\, \beta\, f \tag{4.11}$$

Where d_m is the inner ring mean diameter of the selected bearing. From the knowledge of the p and v, the basic rating life of the component can be finally evaluated from:

$$G_h = b_1\, b_2\, b_3\, b_4\, b_5\, \frac{330}{p^{2.5}\, v} \tag{4.12}$$

Where $b_1 = 2$ for an alternating direction load, $b_3 = 1.18$ is the sliding factor, $b_4 = 1.05$ is the velocity factor, and $b_5 = 1$ is the oscillation factor for $\beta < 5°$.

As a result, each bearing is characterized by a basic rating life of approximately 200 operating hours under the most severe loading conditions, without requiring relubrication. Since the operating conditions adopted for the calculation represent a worst-case scenario that does not reflect the actual duty cycle of the suspension system, which is expected to operate predominantly around the nominal position, the effective service life of each joint is expected to be significantly higher than the calculated rating life. Once the suitability of both joints has been verified, the structural design of the push rod L_2 and the lever L_3 can be addressed in the following section.

4.3 Push rod and lever structural design

Starting from the load conditions evaluated for the push rod and the lever in Section 4.1, the structural design of the linkage components is carried out by determining the minimum allowable geometric dimensions required to ensure mechanical integrity under service conditions. For the lever L_3, the structural dimensioning is performed by evaluating the minimum required moment of inertia of the cross-sectional area with respect to the rotation axis. Under the assumption of linear elastic behaviour and applying Saint-Venant's theory, according to which the minimum moment of inertia of the lever cross section is estimated as a function of the admissible material stress, according to:

$$I_{L_3,min} = \frac{F_{em,max}\, L_3}{\sigma_{adm}}\, y \tag{4.13}$$

where σ_{adm} represents the allowable stress of the selected material, $F_{em,max}$ is the maximum force acting on the lever end, and y is the distance from the axis of rotation of the cross-section local reference frame. The bending moment $F_{em,max} \cdot L_3$ accounts for the distance between the point P and the point B where the force is applied, as depicted in Figure 4.4.

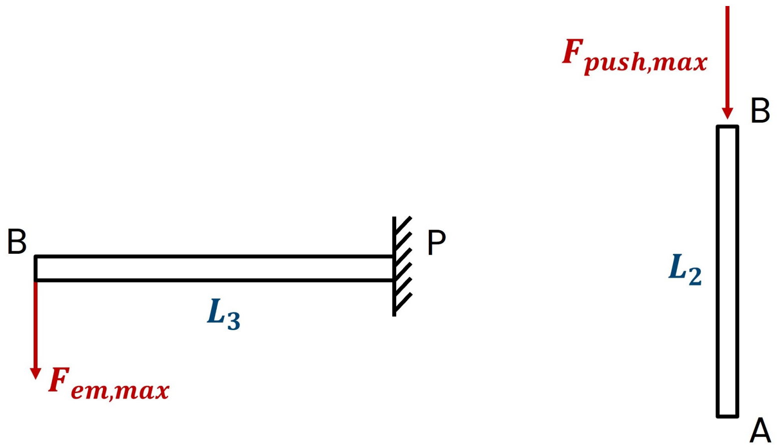

Figure 4.4: Lever and push rod load scheme

For the push rod L_2, the structural sizing is performed assuming a hollow circular cross-section with a fixed internal diameter of $d = 8\,mm$. The component is primarily subjected to axial tensile and compressive loads as shown in Figure 4.4; therefore, the evaluation of the minimum external diameter D is carried out under pure normal stress conditions according to the Saint-Venant theory:

$$D_{L_2,min} = \sqrt{\frac{4\,F_{push,max}}{\pi\,\sigma_{adm}} + d^2} \tag{4.14}$$

The allowable stress used for both push rod and lever preliminary design is evaluated as:

$$\sigma_{adm} = \frac{\sigma_s}{SF} \tag{4.15}$$

where $\sigma_s = 786$ MPa represents the yield strength of the selected steel grade and $SF = 1.5$ is the assumed safety factor, that accounts for uncertainties related to load estimation.

Based on the preliminary analytical sizing methodology just described, the final cross-section geometry of the lever L_3 and the outer diameter of the push rod L_2 have been selected to satisfy the minimum structural requirements. For the lever L_3, an I-shaped cross-section has been adopted, providing a second moment of area higher than the minimum required value, guaranteeing adequate bending stiffness with limited mass increase. For the push rod L_2, an outer diameter of $D = 16$ mm has been selected. This choice allows the realization of M10 threaded ends at the extremities of the tube while maintaining a resistant cross-sectional area greater than the minimum required value, thus ensuring compliance with the admissible stress criterion under axial loading.

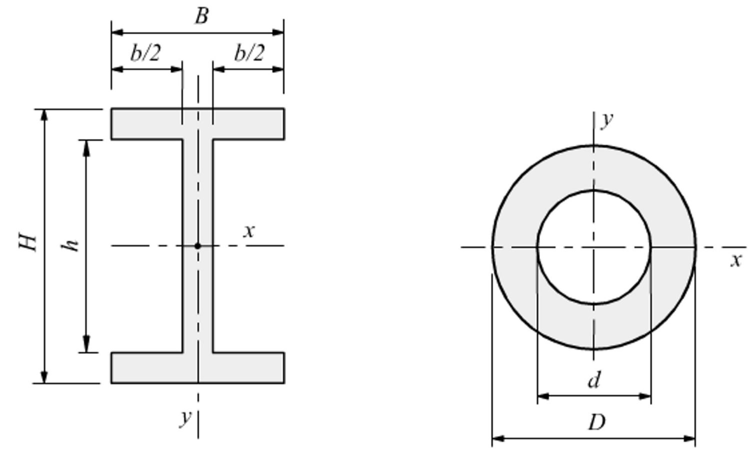

Figure 4.5: Lever and push rod cross sections

With reference to Figure 4.5, the lever cross-section dimensions are defined as: $B =$ 15 mm, $H = 27$ mm, $b = 10$ mm, and $h = 18$ mm in the middle of the lever. The final lever geometry is designed with one cylindrical hub at the hinge P and a fork in the spherical joint B, where the push rod must be connected:

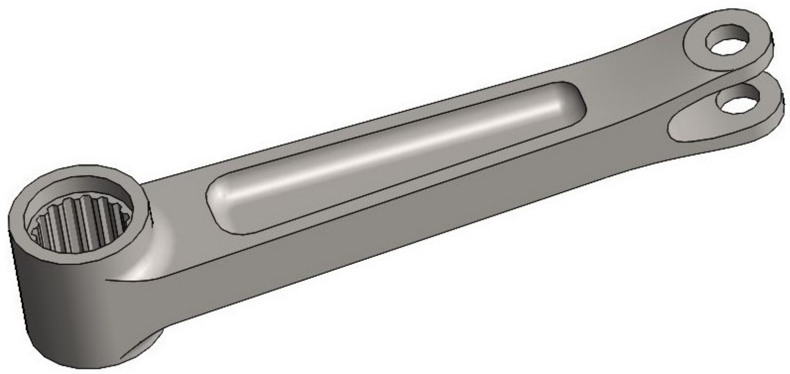

Figure 4.6: Lever final CAD

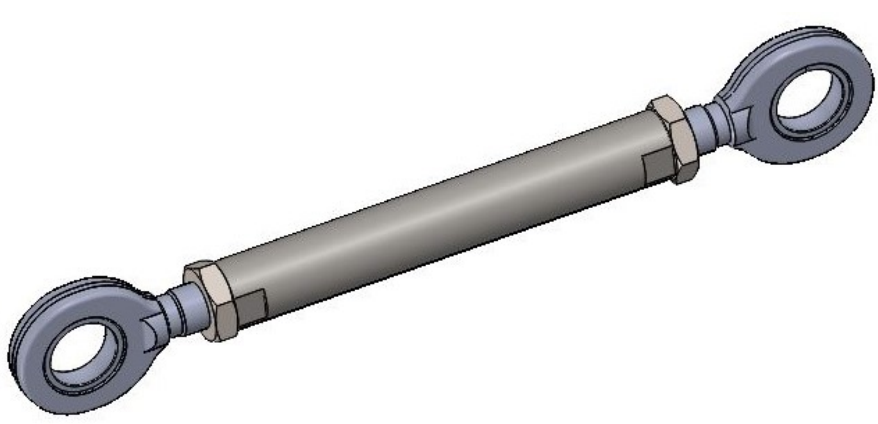

Figure 4.7: Push rod final CAD

As shown in Figure 4.6, the lever L_3 features a variable I-shaped cross-section along its longitudinal axis, that progressively reduces away from the hinge in point P, following the qualitative trend of the bending moment generated by $F_{em,max}$. This solution allows for a more efficient material distribution, leading to a significant weight reduction without compromising the structural integrity of the component. With reference to Figure 4.7, the push rod L_2 is designed to accommodate the selected rod ends through threaded extremities and locking nuts. This configuration allows the axial position of the rod ends to be adjusted and fixed at a prescribed distance, ensuring that the nominal length L_2 defined during the kinematic design phase is accurately achieved and maintained during operation.

Due to its non-uniform geometry and the presence of local discontinuities, the lever L_3 cannot be fully represented by the simplified analytical beam model adopted for preliminary sizing. While the analytical approach provides a reliable estimation of the global bending stresses, it does not account for local stress concentrations arising from three-dimensional effects and load transfer mechanisms at the interfaces. For this reason, a finite element analysis (FEA) has been performed to evaluate the actual stress distribution within the component under the maximum loading conditions identified in the previous sections:

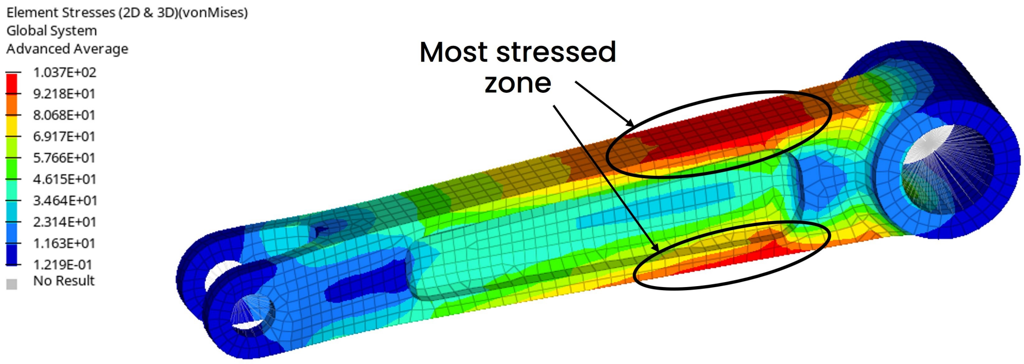

Figure 4.8: Lever finite element analysis (FEA)

The finite element analysis was performed using Altair HyperMesh, and the stress distribution was evaluated according to the von Mises equivalent criterion. The results show a clear stress concentration in the web region of the I-shaped cross-section near the constrained hinge at point P, with a symmetric distribution about the longitudinal axis of the lever. As expected from bending behavior, tensile stresses develop in the upper flange, while compressive stresses arise in the lower flange. It should be noted that this loading configuration represents a worst-case scenario, since rotation about the RRSA axis at the point P is physically constrained in the model, leading to a more severe stress state. Under these assumptions, the maximum equivalent stress reaches approximately $\sigma_{eq,VM} = 104$ MPa in the most critical regions, remaining well below the material yield strength and thus confirming the structural integrity of the component.

Chapter 5

Multibody analysis of the system

In order to further validate the kinematic and dynamic behaviour of the proposed RRSA configuration, a multibody analysis of the complete system has been carried out. While the previous chapters focused on the analytical modelling of the mechanism and on the structural design of the mechanical components, the present study aims at assessing the global behaviour of the system under realistic motion conditions. To this end, the three-dimensional CAD model has been exported and implemented within the multibody simulation environment of Simscape Multibody. This approach enables the mechanism to be represented as an interconnected system of rigid bodies, joints, and constraints, while preserving the actual geometric relationships defined during the design phase. The multibody model is then used to evaluate the evolution of the effective transmission ratio τ throughout the suspension travel, allowing a direct comparison with the analytical results previously derived and thus providing a validation of the methodology presented in Chapter 3.

5.1 Model implementation in Simscape Multibody

After defining all mechanical mates and constraints within the SolidWorks assembly, the model can be exported to the Simscape Multibody environment through the dedicated interface. The correctness and consistency of the imposed mates are essential, as they determine the kinematic structure that is directly transferred to the multibody model. During the export process, each CAD component is converted into a rigid body preserving its mass and inertia properties, while the assembly mates are automatically mapped into the corresponding kinematic joints. This guarantees that the geometric and kinematic relationships defined in the design phase are directly preserved without requiring manual rebuilding of the model. The resulting model is implemented within the Simulink framework as a structured set of interconnected bodies and joints, as shown in Figure 5.1. The actuation is introduced by imposing a rotational motion at the revolute joint of the trailing arm, with the same angular displacements of $\theta_{1,min}$ and $\theta_{1,max}$ adopted in the analytical model. The relevant output quantities are then obtained through dedicated sensor blocks, allowing the angular position at the revolute joint of the lever L_3 and the vertical displacement of the wheel hub to be measured.

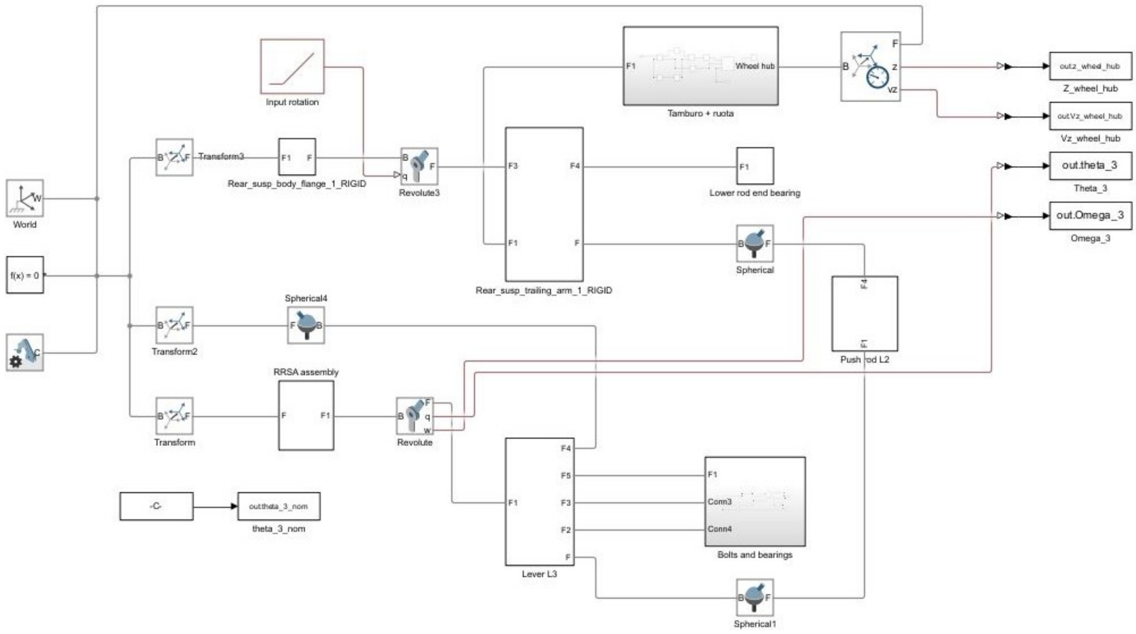

Figure 5.1: Multibody simulink model

The equations of motion of the complete system are then automatically generated and solved by the Simscape solver, enabling the evaluation of the mechanism response under prescribed motion inputs. A three-dimensional animation is then generated, providing a direct visualization of the system (see Figures 5.2 and 5.3).

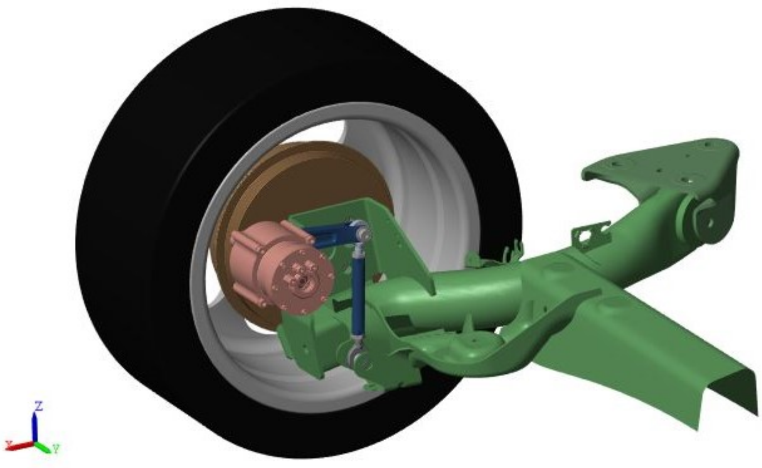

Figure 5.2: Multibody 3D model in nominal position

In this way, the multibody model provides a consistent physical representation of the designed mechanism, preserving the kinematic structure defined during the analytical phase. The implemented framework therefore constitutes the basis for the subsequent evaluation of the transmission parameters and their comparison with the theoretical predictions.

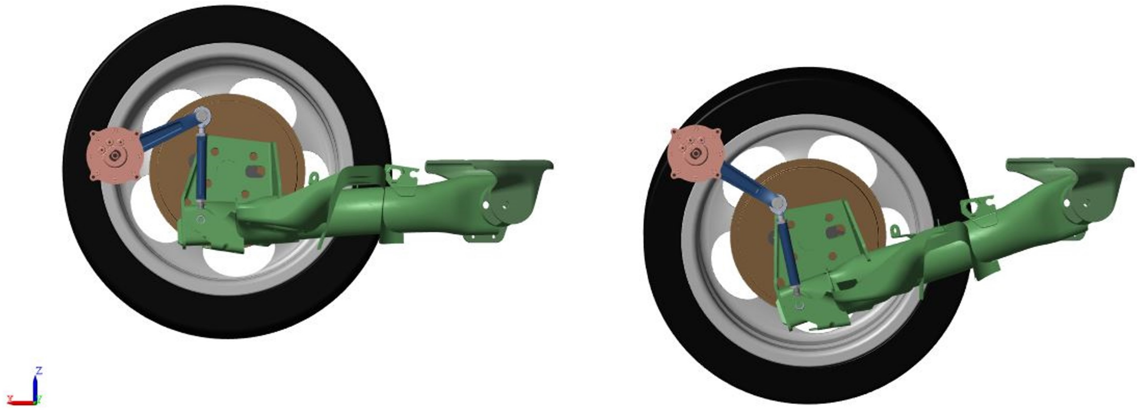

Figure 5.3: Multibody 3D model upper and lower positions

5.2 Results and comparison with the analytical model

The multibody model described in the previous section is now employed to extract the transmission ratio of the selected configuration and to compare it with the analytical prediction derived in Chapter 3. As already explained, the transmission ratio from the wheel hub to the RRSA gearbox input is defined as:

$$\tau_l = \frac{v_{wh}}{\dot{\theta}_{lever}} \tag{5.1}$$

By substituting the output quantities derived from the Simscape Multibody model into Eq. 5.1, the transmission ratio can be evaluated over the same wheel travel range considered in the analytical formulation, while the transmission angle trend can be directly evaluated from the relative orientation between lever and push rod:

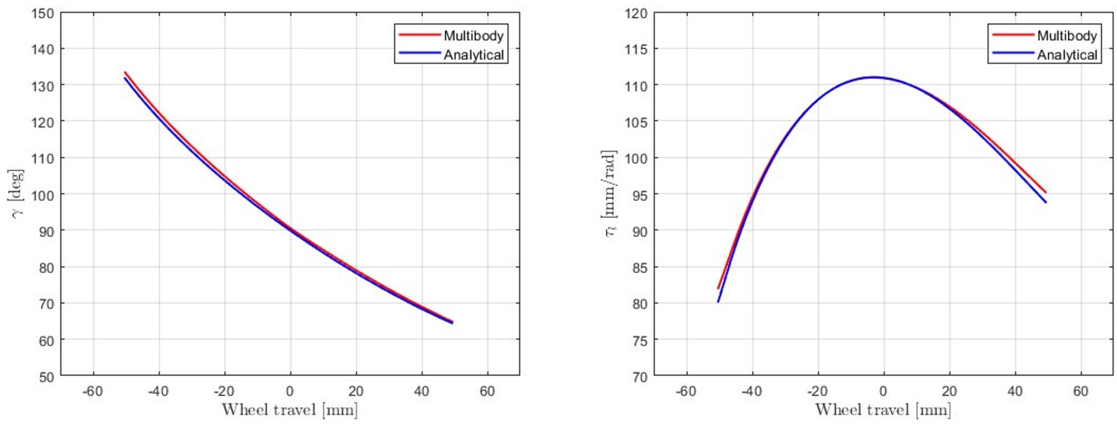

Figure 5.4: Analytical vs multibody results

As can be observed, the trends of the transmission ratio obtained from the analytical and multibody models are nearly coincident in proximity to the nominal suspension position. Slight deviations between the two approaches appear as the suspension moves toward the extreme extension and compression positions. In particular, at the suspension travel boundaries, corresponding to the angles γ_{min} and γ_{max} of the linkage, the transmission ratio computed from the multibody model exhibits slightly higher values compared to the analytical prediction reported in Table 3.8. As a consequence, the deviation of τ_l from its nominal value slightly reduces from $\Delta\tau_l \approx 27\,\%$ of the analytical model to $\Delta\tau_l \approx 25\,\%$, as reported in Table 5.1.

$\boldsymbol{\tau_l}$ and $\boldsymbol{\gamma}$ comparison between analytical and multibody models				
Model	$\boldsymbol{\gamma_{min}}$ $[^\circ]$	$\boldsymbol{\gamma_{max}}$ $[^\circ]$	$\boldsymbol{\tau_l}(\gamma_{\mathbf{min}})$ $\left[\frac{mm}{rad}\right]$	$\boldsymbol{\tau_l}(\gamma_{\mathbf{max}})$ $\left[\frac{mm}{rad}\right]$
Analytical	64.34	131.93	80.04	93.74
Multibody	64.75	133.54	81.89	95.11

Table 5.1: τ_l and γ comparison between analytical and multibody models

Since the suspension system is expected to operate predominantly around the nominal position under normal working conditions, the transmission ratio calculated using the analytical model in Chapter 3 can be considered sufficiently accurate for describing the most frequently operating states of the mechanism. Regarding the transmission angle trend, the two curves remains close to each other, further confirming the validity of the adopted methodology. As final consideration, the slight differences observed in the trends of both objectives between the analytical and multibody models are likely due to the relatively coarse discretization adopted in the analytical model. This discretization was intentionally limited to reduce the computational time required to solve the system for each configuration during the genetic algorithm optimization.

Conclusions and future works

In this work, the optimal integration of a *Rotary Regenerative Shock Absorber* into the rear suspension of a low-voltage reconfigurable battery electric vehicle has been carried out. To this end, the functional and geometric requirements for the optimization problem were defined, considering the kinematic characteristics of the twist beam suspension and the packaging constraints of the vehicle under study. Based on these requirements, a three-dimensional analytical kinematic model of the suspension–actuator system was developed, allowing the mechanism configuration to be evaluated over the entire suspension stroke through the numerical solution of the closure equations. Two possible actuator mounting configurations were investigated, corresponding to a parallel and a perpendicular RRSA orientation with respect to the vehicle longitudinal axis. The analytical model of both configurations was then used to evaluate the objective functions adopted in a *genetic algorithm* to determine the optimal combination of linkage geometry and actuator placement, minimizing the deviation of the transmission ratio from the value determined through quarter-car simulations while keeping a transmission angle as close as possible to 90° in nominal suspension position. The comparison between the parallel and perpendicular actuator mounting orientations led to the selection of the final configuration, considering the variability of the transmission ratio along the suspension travel and the values of transmission angle assumed. Subsequently, the mechanical components of the linkage were designed and verified through CAD modeling and finite element analyses in order to ensure structural integrity while limiting the equivalent mass and inertia of the system. Finally, the complete suspension–actuator system was implemented in a multibody simulation environment, allowing the kinematic and dynamic behavior of the mechanism to be evaluated and compared with the analytical model. The results confirmed the validity of the proposed methodology and the feasibility of integrating the RRSA within the twist beam suspension architecture.

Future works may include the manufacturing of the designed linkage components in order to perform hardware-in-the-loop bench tests of the proposed system, allowing the friction contribution of the joints to be experimentally characterized and compared with the assumptions adopted in the modeling phase. In addition, the development of a suitable control strategy for the effective implementation of the actuator on the vehicle under study will be required, followed by experimental validation through on-road testing. These activities would enable a further assessment of the regenerative capabilities of the system and support the achievement of the objectives defined within the *"MOST Spoke 2: Sustainable Road Vehicles"* project.

Bibliography

[1] G. Genta and L. Morello, "Chapter 3 - Suspensions," in *The Automotive Chassis: Volume 1 – Components Design*, pp. 133–207, Springer, 2009.

[2] G. Genta and L. Morello, "Chapter 23 - Driving dynamic performance," in *The Automotive Chassis: Volume 2 – System Design*, pp. 185–229, Springer, 2009.

[3] G. Genta and L. Morello, "Chapter 25 - Handling performance, Chapter 26 - Comfort performance," in *The Automotive Chassis: Volume 2 – System Design*, pp. 247–428, Springer, 2009.

[4] Gennaro Sorrentino; Renato Galluzzi; Andrea Tonoli; Nicola Amati, "A Generalized Model to Describe Electromagnetic Shock Absorbers," *Engineering Proceedings*, vol. 85, no. 1, p. 11.

[5] M. A. A. Abdelkareem, L. Xu, M. K. A. Ali, A. Elagouz, J. Mi, S. Guo, Y. Liu, and L. Zuo, "Vibration energy harvesting in automotive suspension system: A detailed review," *Applied Energy*, vol. 229, pp. 672–699, Nov. 2018.

[6] M. Yu, S. A. Evangelou, and D. Dini, "Advances in Active Suspension Systems for Road Vehicles," *Engineering*, vol. 33, pp. 160–177, Feb. 2024.

[7] M. Omar, M. M. El-kassaby, and W. Abdelghaffar, "A universal suspension test rig for electrohydraulic active and passive automotive suspension system," *Alexandria Engineering Journal*, vol. 56, pp. 359–370, Dec. 2017.

[8] S. M. Savaresi, C. Poussot-Vassal, C. Spelta, O. Sename, and L. Dugard, "Chapter 2 - Semi-Active Suspension Technologies and Models," in *Semi-Active Suspension Control Design for Vehicles* (S. M. Savaresi, C. Poussot-Vassal, C. Spelta, O. Sename, and L. Dugard, eds.), pp. 15–39, Boston: Butterworth-Heinemann, Jan. 2010.

[9] R. Galluzzi, S. Circosta, N. Amati, and A. Tonoli, "Rotary regenerative shock absorbers for automotive suspensions," *Mechatronics*, vol. 77, p. 102580, Aug. 2021.

[10] X. D. Xue, K. W. E. Cheng, Z. Zhang, J. K. Lin, D. H. Wang, Y. J. Bao, M. K. Wong, and N. Cheung, "Study of art of automotive active suspensions," in *2011 4th International Conference on Power Electronics Systems and Applications*, pp. 1–7, June 2011.

[11] Y. Zhang, H. Chen, K. Guo, X. Zhang, and S. Eben Li, "Electro-hydraulic damper for energy harvesting suspension: Modeling, prototyping and experimental validation," *Applied Energy*, vol. 199, pp. 1–12, Aug. 2017.

[12] L. Zuo and P.-S. Zhang, “Energy Harvesting, Ride Comfort, and Road Handling of Regenerative Vehicle Suspensions,” *Journal of Vibration and Acoustics*, vol. 135, Feb. 2013.

[13] G. Sorrentino, *Design Methodology of Electromagnetic Shock Absorbers for Vehicle Suspensions*. PhD thesis, July 2025. Politecnico di Torino.

[14] S. S. Balli and S. Chand, “Transmission angle in mechanisms (Triangle in mech),” *Mechanism and Machine Theory*, vol. 37, pp. 175–195, Feb. 2002.

[15] J. Gallardo-Alvarado and J. Gallardo-Razo, “Chapter 7 - Generalities,” in *Mechanism: Kinematic Analysis and Applications in Robotics*, pp. 111–134, Jan. 2022.

[16] J. Gallardo-Alvarado and J. Gallardo-Razo, “Chapter 9 - Closed kinematic chains,” in *Mechanism: Kinematic Analysis and Applications in Robotics*, pp. 163–182, Jan. 2022.

[17] Steven C. Chapra, Raymond P. Canale, *Numerical Methods for Engineers*. McGraw-Hill Science/Engineering/Math, sixth ed., 2009.

[18] C. Soares, J. N. van Rijn, J. Vanschoren, and P. Brazdil, *Metalearning for Hyperparameter Optimization*. Switzerland: Springer International Publishing AG, 2022.

[19] Mitchell Melanie, *An Introduction to Genetic Algorithms*. MIT press: Cambridge, 1996.

[20] G. Genta and L. Morello, “Chapter 27 - Control of the chassis and 'By Wire' systems,” in *The Automotive Chassis: Volume 2 – System Design*, pp. 429–495, Springer, 2009.

[21] K. Deb, A. Pratap, S. Agarwal, T. Meyarivan, “A fast and elitist multiobjective genetic algorithm: NSGA-II,” *IEEE Transactions on Evolutionary Computation*, Apr. 2002.

[22] SKF Group, “SKF Spherical Plain Bearings and Rod Ends Catalogue.”